

**Construction and Dynamics of Knotted Soft Matter
Systems**

by

Jack Binysh

Thesis

Submitted to the University of Warwick

for the degree of

Doctor of Philosophy

Mathematics for Real World Systems CDT

....

Contents

Acknowledgments	iii
Declarations	iv
Abstract	v
Chapter 1 An introduction to knotted fields	1
1.1 Kelvin's vortex atom	1
1.2 Modern knotted fields: fluids	5
1.2.1 Călugăreanu's theorem, real fluids	6
1.2.2 Fluids as a case study	8
1.3 Modern knotted fields: liquid crystals	10
1.3.1 A brief introduction to liquid crystals	12
1.3.2 Homotopy theory of knotted disclinations and Pontryagin-Thom surfaces	16
1.3.3 Beyond disclination lines	19
1.4 Modern knotted fields: excitable media	27
1.5 This thesis	36
Chapter 2 Maxwell's Theory of Solid Angle and the Construction of Knotted Fields	40
2.1 Introduction	40
2.2 The homotopy formula for solid angle	43
2.3 Maxwell's geometric formula, dual curves and homotopies along tangent developable surfaces	47
2.3.1 A dual curve theorem for self-intersecting curves	48
2.3.2 The pullback to K and a homotopy along the tangent developable surface	49
2.4 The structure of ω	52

2.4.1	Longitudinal structure — the solid angle framing	52
2.4.2	Transverse structure — curvature induced corrections to ω	55
2.5	Remarks on numerical implementation, extension to links	57
2.5.1	Extension to links	59
2.6	Construction of knotted fields: two illustrations	60
2.6.1	Scroll waves in excitable media	60
2.6.2	Nematic disclinations	61
2.7	Discussion	63

Acknowledgments

Yes Mum I've finished my PhD now. No, I don't know what I'm going to do next.

Declarations

Replace this text with a declaration of the extent of the original work, collaboration, other published material etc. You can use any L^AT_EX constructs.

Abstract

Chapter 1

An introduction to knotted fields

1.1 Kelvin's vortex atom

The original, and perhaps most familiar, example of a knotted field is the smoke ring. Easily made by cutting a circular hole in a rectangular box, then replacing the opposite side entirely with a sheet of rubber, “a blow on this flexible side causes a circular vortex ring to shoot out from the hole on the other side” [Thomson, 1867]. In 1867, exactly this demonstration was shown to Lord Kelvin by Peter Guthrie Tait. What is generated is a tightly circulating tube of air, closed into a ring, which propagates stably across the room, rebounding elastically from walls and even other vortex rings (of course to see the ring one first needs to fill the box with smoke, perhaps using dry ice or “a small quantity of muriatic acid” [Thomson, 1867]). At the time, the microscopic nature of atoms was still under debate, and the stability of the rings, described by Helmholtz’s laws of vortex motion in an ideal fluid [Helmholtz, 1858] (translated into English by Tait), coupled with their elasticity and capacity for internal vibration [Laan, 2012; Lomanaco, 1996] prompted Kelvin to suggest that “Helmholtz’s rings are the only true atoms” [Thomson, 1867]. Kelvin hypothesised that such rings, embedded in a “perfect homogeneous liquid”¹, and “linked together or ... knotted in any manner”² might form the microscopic basis

¹Kelvin did not actually specify whether this fluid was the same as the ‘ether’ hypothesised to transmit electromagnetic waves [Laan, 2012].

²Some terminology: Strictly speaking a knot consists of a single curve, and a link consists of two or more curves. For example, a single round circle is an example of the unknot. Two round circles disconnected from one another is the (two component) unlink. If the two circles threads each other once, we have the Hopf link. We will often be quite loose with the distinction between knots and links.

of matter [Thomson, 1867].

Kelvin’s “vortex atom” encountered difficulties in its mathematical content, its falsifiability, and a lack of contemporary experimental support [Laan, 2012]. However its content, summarised as “*Physics = Geometry*” in Ref. [Lomanaco, 1996], was compelling and apparently motivated Tait, in “consideration of the forms of knots by Sir W. Thomson’s (Lord Kelvin) Theory of Vortex Atoms”, to construct the first systematic tables of knots in 1876–1885, shown in figure 1.1 [Tait, 1876, 1883, 1884]. Tait’s articles, alongside a “very remarkable essay by Listing ... and an acute remark made by Gauss ... with some comments on it by Clerk-Maxwell” [Tait, 1876] form the initial studies in what is now the mathematical field of knot theory [Lickorish, 1997]. Maxwell himself, although not an active contributor to vortex atom theory, had a clear interest in the ideas, encouraging Tait in a letter in 1867 to “prosper and disentangle your formulae in proportion as you entangle your worbles” (figure 1.1). Indeed the “comments by Clerk-Maxwell” referred to by Tait are in fact Maxwell’s re-derivation of Gauss’s linking number, as presented in his *A Treatise on Electricity and Magnetism* [Maxwell, 1873] in 1873, about which we will have much more to say in §2.

Despite forming the starting point for modern knot theory, the knotted structures above are quite different to those found in your shoelaces, or in the world of art and design outside the physics department. Rather than a single knotted curve, we have a continuous fluid in whose structure the knot is encoded, and from which dynamical properties of the knot (its motion, stability, a spectrum of vibrational modes etc.) may be derived. More precisely, we have a concentrated tube of vorticity in the fluid, tied into the shape of a knot. Helmholtz’s laws of vortex motion [Helmholtz, 1858] show that, in a perfect (frictionless) fluid this tube of vorticity is ‘frozen in’ to the fluid, unable to dissipate or cross itself. In an idealised vortex atom, the radius of this tube would tend to zero, with the vorticity contained inside becoming infinite, and we would have a singular linelike structure, tied into a knot and embedded into a continuous three dimensional medium. This structure is our first example of what is called a *knotted field*. There is no strict definition of what constitutes of a knotted field, but a sensible operational one is that they are physical fields containing knotted, linked, or otherwise topologically interesting structure, and that this structure has some interplay with the behaviour of the whole field. As we shall see, such fields are certainly not confined to fluids.

The disconnect between a knotted curve and a knotted field is reflected in Tait’s work, which mentions Kelvin’s Vortex Atoms briefly as motivation, but focuses in substance on “the investigation of the essentially different modes of joining

a

GLENLAIR
DALBEATTIE,
Nov. 13, 1867.

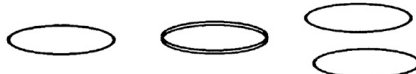
Dear Tait

If you have any spare copies of your translation of Helmholtz on "Water Twists" I should be obliged if you could send me one.

I set [sic] the Helmholtz dogma to the Senate House in '66, and got it very nearly done by some men, completely as to the calculation, nearly as to the interpretation.

Thomson has set himself to spin the chains of destiny out of a fluid plenum as M. Scott set an eminent person to spin ropes from the sea sand, and I saw you had put your calculus in it too. May both prosper and disentangle your formulae in proportion as you entangle your worbles. But I fear the simplest indivisible whirl is either two embracing worbles or a worble embracing itself.

For a simple closed worble may be easily split and the parts separated



but two embracing worbles preserve each others solidarity thus



though each may split into many, every one of the one set must embrace every one of the other. So does a knotted one.



yours truly

J. CLERK MAXWELL

b

two closed curves and/or the distance between them and of $\text{C} \cdot m \cdot n$, $\text{d} \cdot m \cdot v$, and $L \cdot M \cdot N$ are the direction cosines of $\text{d} \cdot s$ and $\text{d} \cdot v$ respectively,

then $\int \frac{ds}{dr} \left[\frac{L \cdot M \cdot N}{r \cdot d \cdot m \cdot n} \right]$

$$= \int \frac{ds}{dr} \left[\left(1 - \frac{dx}{ds} \right) \left(1 - \frac{dy}{ds} \right) - \left(\frac{dx}{ds} \right)^2 \right]^{\frac{1}{2}}$$

$$= 4\pi n$$

the integration being extended round both curves and n being the algebraic number of times that one curve embraces the other in the same direction.

If the curves are not linked together $n = 0$ but if $n = 0$ the curves are not necessarily independent.

1 8 2 3

In fig 1 the two closed curves are inseparable but $n = 0$. In fig 2 the 3 closed curves are inseparable but $n = 0$ for every pair of them. Fig 3 is the simplest knot and an unsymmetrical curve. The simplest equation I can find for it is $r = b + a \cos^2 \theta$ $z = c \sin \frac{\theta}{2}$ when c is $-ve$ as in the figure the knot is right-handed when c is $+ve$ it is left-handed. A right-handed knot cannot be changed into a left-handed one

c

422.] VECTOR-POTENTIAL OF A CLOSED CURVE. 41

to be intertwined alternately in opposite directions, so that they are inseparably linked together though the value of the integral is zero. See Fig. 4.

It was the discovery by Gauss of this very integral, expressing the work done on a magnetic pole while describing a closed curve in presence of a closed electric current, and indicating the geometrical connexion between the two closed curves, that led him to lament the small progress made in the Geometry of Position since the time of Leibnitz, Euler and Vandermonde. We have now, however, some progress to report, chiefly due to Riemann, Helmholtz and Listing.

422.] Let us now investigate the result of integrating with respect to r round the closed curve.

One of the terms of Π in equation (7) is

$$\frac{\xi - z}{r^3} \frac{d\eta}{ds} \frac{dz}{ds} = \frac{d\eta}{ds} \frac{d}{ds} \left(\frac{1}{r} dz \right). \quad (8)$$

If we now write for brevity

$$F = \int \frac{1}{r} \frac{dz}{ds} ds, \quad G = \int \frac{1}{r} \frac{dy}{ds} ds, \quad H = \int \frac{1}{r} \frac{dx}{ds} ds, \quad (9)$$

the integrals being taken round the closed curve s , this term of Π may be written

$$\frac{d\eta}{ds} \frac{d^2 H}{d\xi ds},$$

and the corresponding term of Π will be

$$\frac{d\eta}{ds} \frac{dH}{d\xi}.$$

Collecting all the terms of Π , we may now write

$$-\frac{d\omega}{ds} = -\int \Pi ds = \left(\frac{dH}{d\xi} - \frac{dG}{ds} \right) \frac{d\xi}{ds} + \left(\frac{dF}{d\xi} - \frac{dH}{d\eta} \right) \frac{d\eta}{ds} + \left(\frac{dG}{d\xi} - \frac{dF}{d\eta} \right) \frac{d\xi}{ds}. \quad (10)$$

This quantity is evidently the rate of decrement of ω , the magnetic potential, in passing along the curve s , or in other words, it is the magnetic force in the direction of ds .

By assuming ds successively in the direction of the axes of x , y and z , we obtain for the values of the components of the magnetic force

d

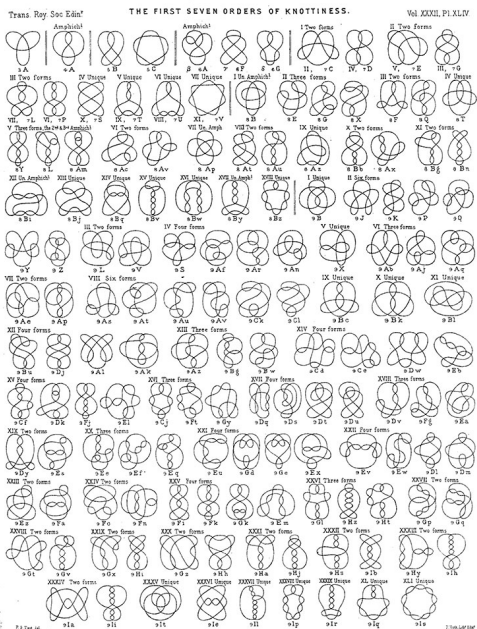


Figure 1.1: (a) 1867. Letter from Maxwell to Tait, encouraging him to "prosper and disentangle your formulae in proportion as you entangle your worbles" and requesting Tait's own translation of [Helmholtz, 1858]. (b) 1867. Letter from Maxwell to Tait, showing a formula for Gauss's linking number alongside two links of linking number 0 and a trefoil knot. Reproduced from Ref. [Ricca and Nipoti, 2011]. (c) 1873. Page from Maxwell's *A Treatise on Electricity and Magnetism* [Maxwell, 1873], giving a discussion of the Gauss linking number and the same example of linking number zero seen in (b). (e) 1876. The first iteration of Tait's knot tables [Tait, 1876].

points in a plane” [Tait, 1876]. As knot theory developed, its initial connections to hydrodynamics and electromagnetism were further abandoned. One also notes that despite the wonderful knot tables produced by Tait (figure 1.1) and the reliance of vortex atom theory on knotted and linked vortices, there is no mention above of any experimental evidence of vortices tied in nontrivial knots.

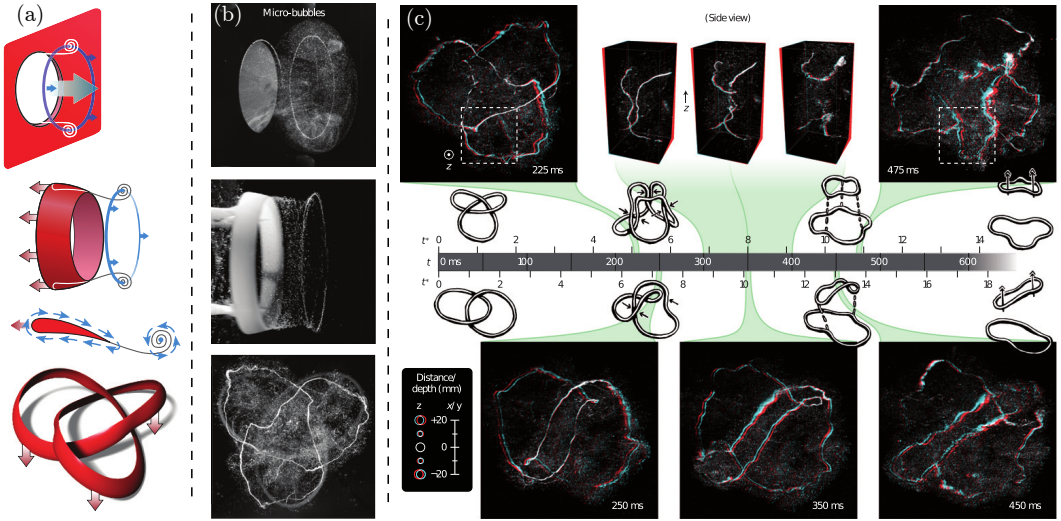


Figure 1.2: The first experimental construction of fluid knotted vortices, in 2013. (a) Experimental methods for making knotted vortices. The hydrofoil (bottom three panels) is most successful. (b) Vortices produced in water from the designs of panel (a). Microbubbles track the vortex. The mean radius of the ring is 40mm, of the trefoil 45mm. (c) Timelines showing the evolution of a trefoil knot (top) and Hopf link (bottom) in three dimensions. In contrast to ideal fluids, we see progressive reconnections and simplification of the links. Figures reproduced from Ref. [Kleckner and Irvine, 2013].

The first experimental construction of nontrivial knotted fluid vortices came 146 years after their initial theoretical investigation, from the Irvine lab in 2013. We show in figure 1.2 several remarkable figures reproduced from Ref. [Kleckner and Irvine, 2013], in which Kleckner and Irvine tied a single vortex loop in water into a trefoil knot, the simplest nontrivial knot, as well as linking two vortex loops together (Kelvin’s proposed model for a sodium atom), before tracking their full three-dimensional evolution. Ref. [Kleckner and Irvine, 2013] is a notable example of a more general trend; over the past ~ 10 years knotted fields have gone from being purely theoretical constructions to being experimentally realisable in a number of systems, and though originally conceived of in fluid dynamics, modern applications are not limited to this context; they have been realised as nodal lines of optical beams [Dennis et al., 2010], as disclinations in nematic liquid crys-

tals [Tkalec et al., 2011; Tasinkevych et al., 2014; Čopar et al., 2015] and as spinor Bose-Einstein condensates [Hall et al., 2016]. In the following sections we will review the state of modern experiment and theory on knotted fields, beginning with fluids and superfluids, in some sense the most developed case, before moving on to parallel developments in liquid crystals and excitable media, which directly underlie the work presented in §?? and §?? in this Thesis; these example are certainly not exhaustive, and focus on ‘soft matter’ systems, a point we shall discuss at the end of the chapter. We shall see that the subject has broadened considerably since Kelvin’s atoms and his contemporaries’ study of fluids. There will be a commonality of ideas between the different disciplines mentioned above, but also genuine differences.

1.2 Modern knotted fields: fluids

With the decline of Kelvin’s vortex atom theory and the development of knot theory away from its hydrodynamic origins, a resurgence of interest in knotted fields might be dated to the years 1958-1969, with Moreau and Moffatt’s seminal papers on helicity in ideal fluids [Moreau, 1961; Moffatt, 1969], preceded by analogous results in magnetohydrodynamics by Woltjer [Woltjer, 1958]. Focusing on the ideal fluid, both Moreau and Moffatt independently demonstrated that the helicity

$$\mathcal{H} = \int \mathbf{u} \cdot \boldsymbol{\omega} \, d^3\mathbf{r}, \quad (1.1)$$

where $\mathbf{u}(\mathbf{r}, t)$ is the fluid velocity and $\boldsymbol{\omega} = \nabla \times \mathbf{u}$ is the vorticity [Saffman, 1992], is conserved under the Euler equations of ideal flow. Moffatt in particular gave this invariant a topological interpretation: it measures the linking of vortex tubes within the fluid. Given a fluid where $\boldsymbol{\omega}$ is concentrated along discrete sets of curves C_i , Moffatt showed that

$$\mathcal{H} = \sum_{i,j} \Gamma_i \Gamma_j Lk(C_i, C_j) \quad (1.2)$$

where Γ_i is the vorticity flux along curve C_i , and $Lk(C_i, C_j), i \neq j$, is the Gauss linking number between curves C_i, C_j (this interpretation of helicity actually extends to the case where the vorticity is not concentrated along a finite set of curves, but is distributed throughout the fluid [Arnold and Khesin, 1999]). The meaning of $Lk(C_i, C_j)$ will be clarified below. Figure 1.3 shows several examples of vortex tubes with different linking numbers and hence helicities. Seen in this light, the conservation of helicity is a direct consequence of Helmholtz’s laws of vortex motion, and is equivalent to the statement that initially linked vortex tubes remain so; in some sense it is remarkable that the result was not known to Kelvin and Maxwell.

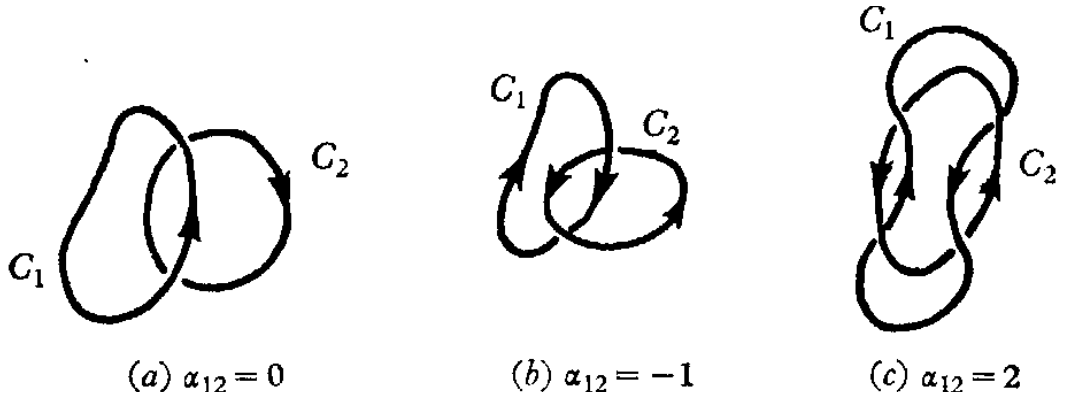


Figure 1.3: Three examples of links with different linking numbers. In the figure, $Lk(C_i, C_j)$ is denoted α_{ij} . Figure reproduced from Ref. [Moffatt, 1969].

When vorticity is not concentrated along a singular curve but distributed in a thin vortex tube, there is additional internal structure — one imagines a ribbon (figure 1.4(a)), or braided rope (figure 1.4(b)). Flux lines may wind around the centre-line of this tube as in figure 1.4(b), endowing it with a second linking number, the self-linking number, which measures the linking of any flux line with the curve centre-line. Incorporating this structure into the helicity count we find [Moffatt and Ricca, 1992]

$$\mathcal{H} = \sum_{i,j,i \neq j} \Gamma_i \Gamma_j Lk(C_i, C_j) + \sum_i \Gamma_i^2 SL(C_i), \quad (1.3)$$

where $SL(C_i)$ denotes the self-linking of each curve C_i with its implicitly assumed ribbon. Defining $Lk(C_i, C_i) := SL(C_i)$ this expression reduces to (1.2). In Ref. [Moffatt, 1969] Moffatt does not explicitly consider a vortex tube, but nevertheless defines a ‘self winding number’, which with the benefit of hindsight one interprets as the self-linking number of the simplest kind of tube, one made up of a family flux lines running parallel to one another. As we shall see below, that the flux lines are locally parallel does not imply $SL(C_i) = 0$.

1.2.1 Călugăreanu’s theorem, real fluids

Given a ribbon diagram like figure 1.4(a), the self-linking number may be further decomposed as

$$SL = Tw + Wr. \quad (1.4)$$

The first term, the twist Tw , counts the local crossings of the ribbon over its centre-line. The second term, the writhe Wr , counts non-local crossings of the ribbon over distant parts of the centre-line. In figure 1.4 each crossing of the ribbon over

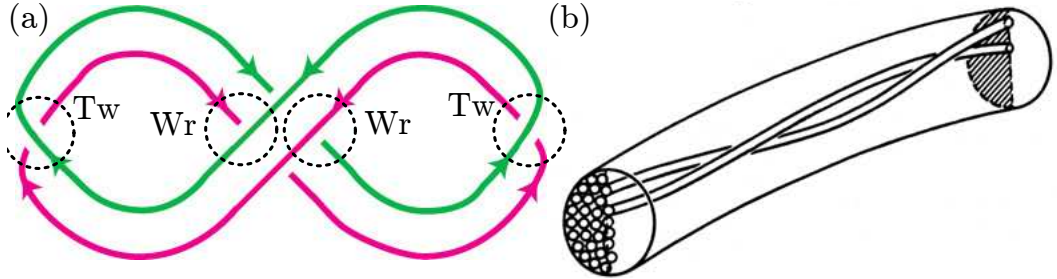


Figure 1.4: A curve with internal structure: ribbons and tubes. (a) A ribbon, defined by a centre-line (pink, say) and a second offset curve (green). The diagram is a projection of the ribbon living in three dimensions, and each crossing may be annotated as either a twist Tw or writhe Wr crossing, depending on its local (green across pink, no pink across pink) or nonlocal (green across pink + pink across pink) nature. The total count gives a self-linking number for the ribbon; see (1.4). (b) A twisted tube, in which one particular ‘filament’ may be arbitrarily chosen to define a ribbon. This is the situation in vortex tubes. Figures reproduced (modified) from Refs. [Dennis and Hannay, 2005; Moffatt and Ricca, 1992].

its centre-line is annotated with the nature of its contribution. Note that the Wr count is actually independent of the choice of ribbon. For different diagrams of the same knotted ribbon each of these contributions varies, but their sum SL does not. Averaging over also possible diagrams, i.e. all possible projections of the genuine three-dimensional curve, one obtains integral formulae for twist and writhe, and in this form the result (1.4) was first discovered by Georges Călugăreanu [Călugăreanu, 1959, 1961] (the interpretation of it given above is however due to Ref. [Dennis and Hannay, 2005]). Călugăreanu’s Theorem is an important and influential result, finding application in Mathematics, Physics, Biology and beyond. It is of potential relevance whenever one studies the properties of a curve with some internal structure, and so it naturally appears frequently in the study of knotted fields. It will play a role in the curve dynamics studied in §??, in conservation laws encountered in §?? and, in its close connection to Maxwell and Gauss’s work on linking numbers and electromagnetism, in §2 as well. For the purposes of the current discussion it enables us to speak of writhe helicity Wr and twist helicity Tw , two separate contributions to the total helicity count. All three modes of helicity storage are shown in figure 1.5(a). Assuming all vortices in the system have the same flux Γ we have that

$$\mathcal{H} = \Gamma^2 \sum_i \sum_{j \neq i} Lk(C_i, C_j) + Tw(C_i) + Wr(C_i). \quad (1.5)$$

To return again to Moffatt's original result (1.2), a locally parallel bundle of tubes has $Tw(C_i) = 0$, and only contains writhe helicity, as in the Wr component of figure 1.5(a) — in other words here $SL(C_i) = Wr(C_i)$. In this case (1.5) reduces to (1.2). Consistent with this fact, $Wr(C_i)$ may be computed from the curve C_i only, without the need to explicitly consider a tube at all (further, the integral formula for the Gauss linking number reduces to the integral formula for writhe when the curves involved coincide [Moffatt and Ricca, 1992]), and so if one neglects internal tube structure they will pick up the Wr but not the Tw contributions to helicity; this is referred to as the centre-line helicity $\mathcal{H}_c := Lk + Wr$ [Scheeler et al., 2014].

In a real (viscous) fluid, helicity is not *a priori* conserved. The question of whether it is in practice, and the mechanism of its dissipation, are areas of active research [Kleckner and Irvine, 2013; Scheeler et al., 2014, 2016]. Naively, one expects the reconnections shown in figure 1.2 to be accompanied by jumps in the value of helicity. Ref. [Scheeler et al., 2014] measured the centre-line helicity \mathcal{H}_c across reconnections in trefoil knots and Hopf links, as shown in figure 1.5(b). They found that \mathcal{H}_c is in fact not dissipated in a reconnection, but rather transferred from Lk to Wr . Ref. [Scheeler et al., 2016] measured all three contributions to \mathcal{H} including Tw in a system of unlinked rings, finding Tw to be dissipated by viscosity, but the remaining contribution \mathcal{H}_c preserved (figure 1.5(c)). Taken together the results suggest that helicity is primarily dissipated on small scales via the Tw term, and not by reconnections as might have been expected — this leads to approximate conservation of helicity over surprisingly long timescales.

1.2.2 Fluids as a case study

The hydrodynamic (and magnetohydrodynamic) story of knotted fields is well developed. We have given a sketch, but the reader is invited to find more detail in reviews such as Refs. [Moffatt, 2014; Irvine, 2018]. Outside of hydrodynamics the above discussion acts as a template for what one might expect in knotted fields more generally; a test case which other systems may be compared to and contrasted against. In particular, linking and self-linking of structure occur in a variety of contexts, and in analogy to (1.5) one might seek to connect them to conserved quantities, and use them to understand the dynamics of the entire system under study. To give a brief example of a system for which this template is fruitful consider superfluids, close cousins of normal fluids described by a complex scalar field $\psi = |\psi|e^{i\phi}$ (figure 1.6(a)) evolving via the non-linear Schrödinger equation [Kleckner et al., 2016]. Here vortices are given by singular lines where the circle-valued phase field ϕ is undefined, and about which it winds by 2π . As in fluids, one may define a notion of helicity,

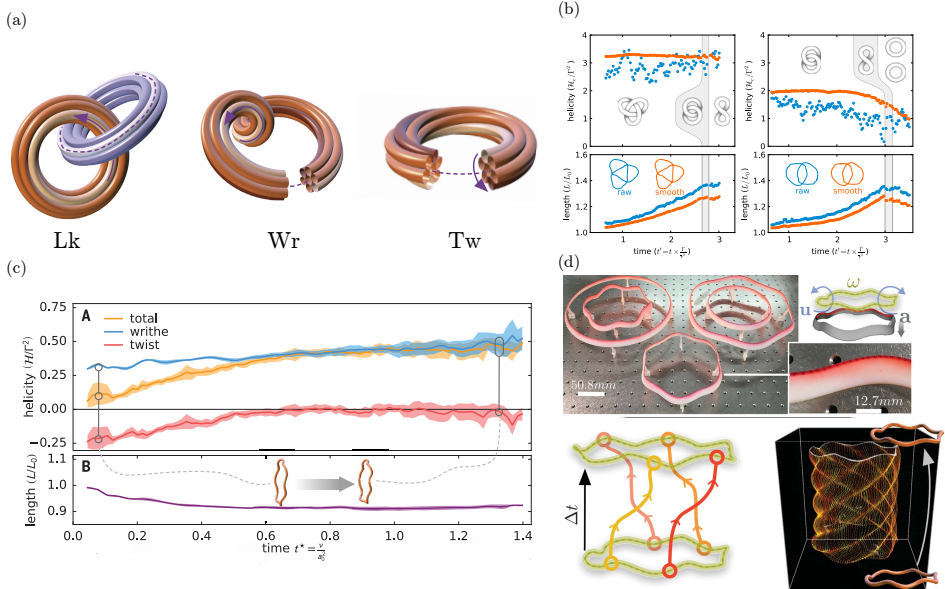


Figure 1.5: Evolution of helicity in a viscous fluid. (a) The three modes of helicity storage: linking Lk of two vortex tubes, writhing Wr of the centre-line of a single tube, and twisting Tw of the vortex tube about the centre-line. (b) Experimental data (blue curves raw data, orange curves smoothed) tracking centre-line helicity $\mathcal{H}_c := Lk + Wr$ evolution for a trefoil knot and Hopf link, showing that \mathcal{H}_c is conserved across reconnections. (c) The three contributions to helicity are experimentally tracked as a vortex ring evolves. Twist helicity Tw dissipates to zero, but writhe helicity Wr is conserved. (d) The experimental setup allowing the measurements shown in panel (c). Tangential flow resolution along the vortex core is enabled by impregnating an aerofoil with separated blobs of dye, which are traced over time. Figures reproduced from Refs. [Scheeler et al., 2014, 2016].

initialise knotted vortices and study their evolution (figure 1.6(b)) [Scheeler et al., 2014; Kleckner et al., 2016]. The definition of centre-line helicity $\mathcal{H}_c := Lk + Wr$ carries through, and its evolution turns out to be similar to that of viscous fluids [Scheeler et al., 2014; Kleckner et al., 2016]; reconnections occur in similar manner, and they approximately preserve the centre-line helicity \mathcal{H}_c .³

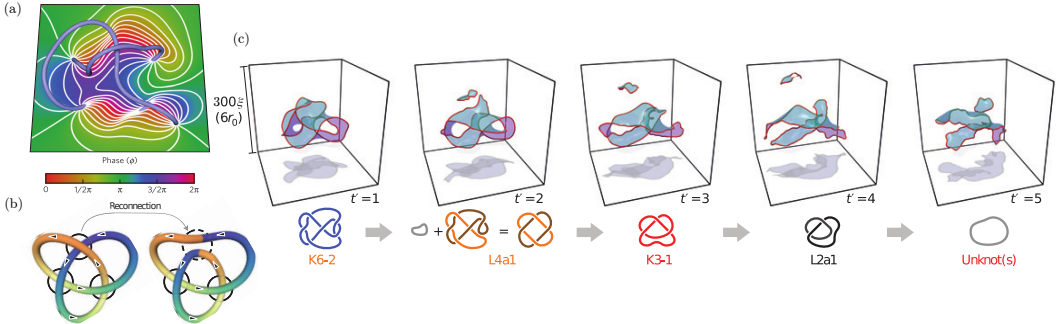


Figure 1.6: Evolution of superfluid vortex knots. (a) Cross section through a superfluid vortex knot (light blue curve), showing the phase field ϕ winding by 2π about the vortex. (b) A schematic illustration of a reconnection. Colour is for visualisation only; note the splicing. (c) An example untying of a superfluid link into a collection of unknots by progressive reconnections. Blue surfaces spanning the knot are surfaces of constant phase. A schematic of the untying process is shown below.

However, it is not the case that knotted fields in all other systems may be understood simply through the lens of fluids. In the following section we turn to the second experimental system with which substantial work on knotted fields has been done, the nematic liquid crystal cells of Refs. [Tkalec et al., 2011; Tasinkevych et al., 2014; Čopar et al., 2015]. There will be some crossover with the discussion above, but also genuine differences, especially in the theoretical constructions involved.

1.3 Modern knotted fields: liquid crystals

A second experimentally constructed knotted field is shown in figure 1.7. It is quite different to that of figure 1.2. By including microscopic colloids a few μm wide into a thin cell of nematic liquid crystal, experimentalists [Tkalec et al., 2011; Tasinkevych et al., 2014; Čopar et al., 2015] are able to force the appearance of defect lines in the material. These defects may then be manipulated with laser tweezers, and by

³ Construction of the full helicity \mathcal{H} is harder: the natural ribbon structure for a single superfluid vortex is given by its intersection with the surface $\phi = 0$, the ‘Seifert framing’ [Winfrey and Strogatz, 1983c; ed. H. K. Moffatt ed., 1992] for which $\mathcal{H} = 0$! See [Hänninen et al., 2016; Salman, 2017; Kedia et al., 2018b] for a resolution to this apparent paradox. We will encounter Seifert framings again, canonically constructed by the solid angle function, in §2.

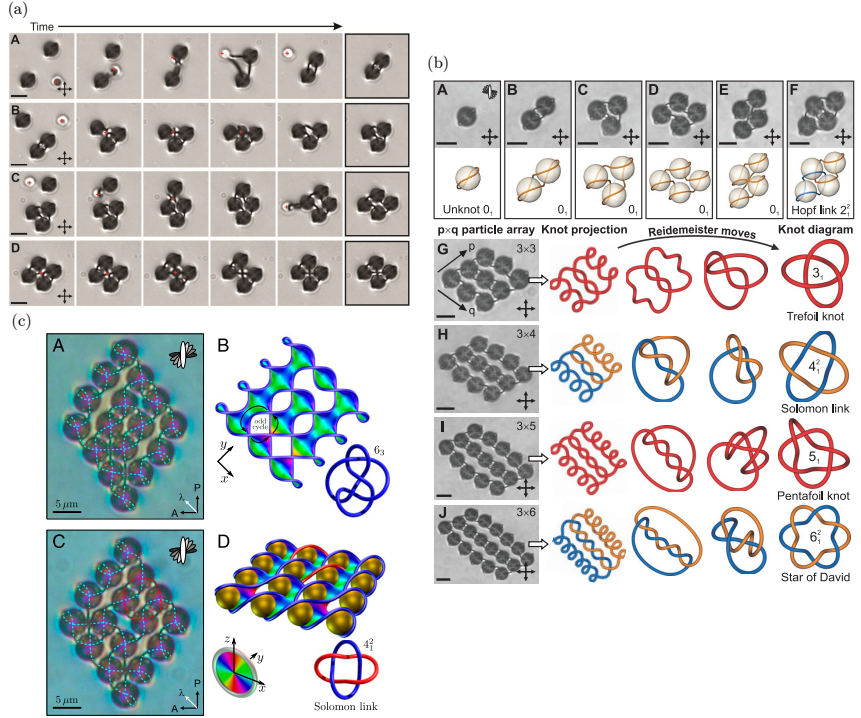


Figure 1.7: Knotted disclination lines. (a) Nematic disclinations (dark curves) are wrapped around silica colloids $4.82 \mu\text{m}$ in diameter (dark spheres), initially in ‘Saturn’s ring’ configurations. Both disclinations and colloids may be manipulated by laser tweezers (red dot). The figure shows controlled assembly of an array of colloids with a single defect line wrapped about them. Black scale bar $5 \mu\text{m}$. (b) Any knot or link may be constructed around these colloidal arrays. The figure shows the experimental assembly of a Hopf link alongside simulation predictions of its shape at each stage, as well as several other completed knots and links. (c) Within two finished links, the sense in which the director \mathbf{n} is twisting is shown with colouring: the background dark blue corresponds to one handedness, with regions of light colour denoting its reversal. This visualisation allows construction of the Pontryagin-Thom (PT) surface for the link, which in turns allows homotopy classification (1.6). Figures reproduced from Refs. [Tkalec et al., 2011; Čopar et al., 2015].

weaving them about an array of colloids, a knotted field encoding any type of knot or link can be constructed; unlike the fluid vortices above, these structures are stable, able to be experimentally probed in some detail. This system provides a testbed for a series of new ideas about knotted fields, but first we step back a moment and provide a brief description of what liquid crystals, defects and colloids etc. actually are.

1.3.1 A brief introduction to liquid crystals

Liquid crystals are a class of materials which possess properties associated to both liquids and solids [de Gennes and Prost, 1996]. In their most common form, the nematic phase, they show no positional order, and flow like a liquid. However, they do show orientational order: if one attempts to twist a portion of the liquid crystal it will respond elastically, as a solid would⁴. The microscopic basis for this behaviour comes from the type of molecules which comprise nematics, two examples of which are shown in figure 1.8(a)–(b); they are typically thin rods which locally align themselves along some common axis without taking on any sort of crystalline positional order. In continuum theories this orientational order is described by a spatially varying unit vector field \mathbf{n} , called the director, which represents an average local molecular orientation, as shown in figure 1.8(c).

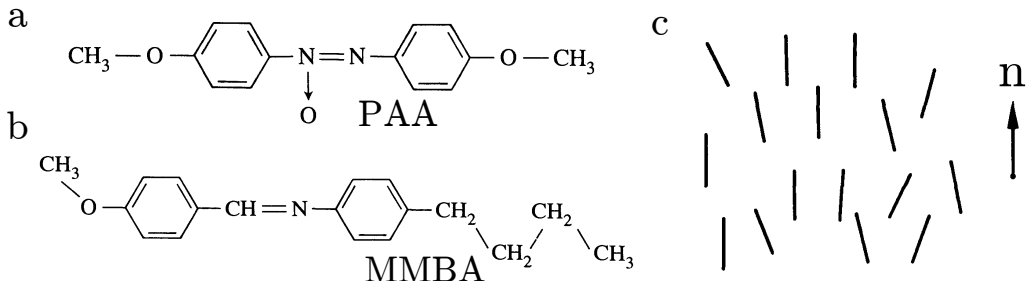


Figure 1.8: (a,b) Two example of molecules which can form a nematic liquid crystalline phase. (a) p-azoxyanisole (PAA) forms a nematic between 116–135°C at atmospheric pressure. (b) N-p-methoxybenzylidene-p-butylanilinie (MMBA) forms a nematic between 20–47°C. (c) A schematic of local molecular alignment, with the director \mathbf{n} giving a direction averaged over microscopic lengthscales. Figures reproduced (modified) from Ref. [de Gennes and Prost, 1996]

The theory of their elastic distortions contains much interesting geometry

⁴This is remarkable: imagine your surprise if, upon attempting to stir your coffee, you found it fiercely resisted your attempts to turn the spoon, but was nevertheless happy to be poured down the sink.

which we will return to in §1.3.3, but for an understanding of figure 1.7 we instead focus on a celebrated feature of nematics [Frank, 1958], their topological defects. If one shines polarised light through a thin slice of nematic placed between crossed polarisers, they will observe something like figure 1.9 (a), a schlieren texture⁵ [de Gennes and Prost, 1996]. Places in the sample where the director \mathbf{n} is aligned with one of the two polariser directions H and V do not transmit light, leading to the dark brushes observed. One immediately notes points where the brushes meet, sometimes with two brushes leading into a point, sometimes four; a point of each type is marked in figure 1.9(a). What is the structure of the director at these points? The confluence of dark brushes implies that, in a small circle around these points, the director winds, and that at the point itself we cannot consistently define \mathbf{n} ; these points are topological defects, places where the order breaks down. Traversing such a circle around a point with two brushes, the director is aligned with each of H and V only once; in other words it makes only half a turn in a full circle around the defect. This observation is enough to establish that the director \mathbf{n} must in fact be non-orientable; it should not be thought of as a vector field, but as a line field, for which $\mathbf{n} \sim -\mathbf{n}$. In figures 1.9(b)–(e) we show qualitative configurations of the director around these defects, with their associated schlieren texture brushes. In figures 1.9(b),(e) we have four brushes, and a line field which can be oriented; to emphasise this fact we have decorated the line field with one of the two possible choices of arrowheads. Figures 1.9(c),(d) correspond to the non-orientable two brush case; here one cannot consistently assign arrowheads to the rods (it is worth trying to imagine doing so). Note that from a single image such as figure 1.9(a), we cannot distinguish defects winding in a right handed sense ($+ \frac{1}{2}, +1$ etc. in the figure) from left handed by counting brushes. In two dimensions these defects, also called disclinations or disinclinations [Frank, 1958], are points, but in three dimensions they are lines, transverse cross sections of which have local profiles resembling the two dimensional case; a schematic illustration is shown in figure 1.9(f). As with fluid vortices, these disclination lines may be knotted and linked together, and the variation of the local profile along the disclination (see the cross sections in figure 1.9(f)) provides internal structure giving rise to self-linking [Čopar and Žumer, 2011].

Experiments on knotted disclination lines

We now return to the experiments of Refs. [Tkalec et al., 2011; Tasinkevych et al., 2014; Čopar et al., 2015]. In contrast to the situation in fluids, one of the major advantages of working with liquid crystal disclinations is the control experimentalists

⁵The word ‘texture’ is commonly used to describe liquid crystal configurations more generally.

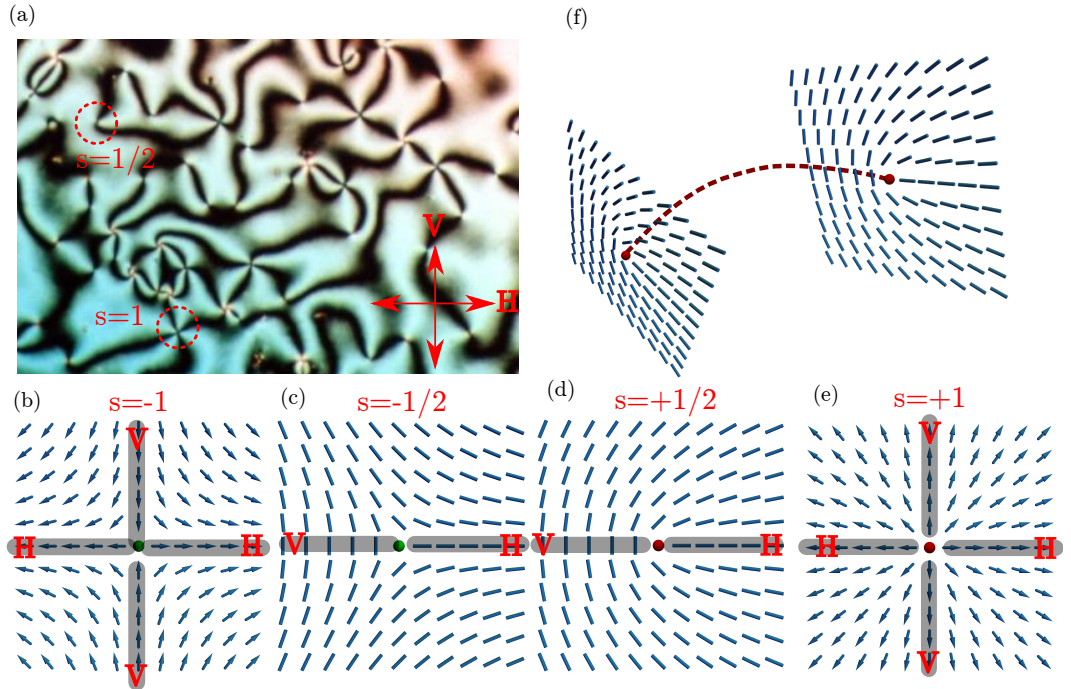


Figure 1.9: Topological defects in liquid crystals. (a) A schlieren texture, with crossed polariser directions overlaid, and defects of winding number (denoted s) $\frac{1}{2}$ and 1 highlighted (one cannot distinguish \pm from the picture alone). (b)–(e) Topologically accurate director configurations around defects of winding number $\pm\frac{1}{2}$, ± 1 , with the schlieren dark brushes overlaid. For ± 1 defects it is possible to orient the director, and we have made one of the two possible choices of arrowheads. (f) Schematic of a disclination line in a three-dimensional nematic sample, with two cross sections showing local structure. Locally, there is only one type of disclination line ($\pi_1(\mathbb{R}P^2) \approx \mathbb{Z}_2$) so a winding is not given.

have over them. By including microscopic silica spherical colloids ($4.72\ \mu\text{m}$ diameter in figure 1.7) into a sample of liquid crystal with specific surface anchoring conditions, experimentalists may frustrate alignment of the director \mathbf{n} in a controlled fashion, necessitating the appearance of disclination lines. For example, in a thin cell of liquid crystal treated to promote uniform alignment of \mathbf{n} within the sample, the inclusion of a colloid with normal anchoring conditions forces the appearance of a defect line around it to cancel the colloid’s topological charge (it effectively acts as a point defect) and allow \mathbf{n} to relax to uniform at large distances. Two such “Saturn’s ring” configurations may be seen in the first frame of figure 1.7(a). Once generated, these disclinations, as well as the colloids they wrap around, may be further manipulated using laser tweezers [Tkalec et al., 2011], as shown in the remainder of figure 1.7(a). When two of these colloids are brought together the disclinations, either spontaneously or induced by the tweezers, fuse together (figure 1.7(a), top row). Assembling an array of these colloids and weaving the disclination lines around them, the setup of Refs. [Tkalec et al., 2011; Tasinkevych et al., 2014; Čopar et al., 2015] allows targeted construction of any knot or link; examples of some possible link topologies are shown in figure 1.7(b). This system strikingly illustrates that knotted fields have more structure than a single knotted curve — the curve organises the entire field (in this case the director \mathbf{n}) around it. Figure 1.7(c) shows the knotted liquid crystal coloured by whether the director is twisting in a right or left handed sense. We see that the disclinations separate the liquid crystal into alternately right and left handed regions. In fact this division allows construction of a surface spanning the disclinations called the Pontryagin-Thom (PT) surface [Chen, 2012; Chen et al., 2013], shown as the coloured surfaces in figure 1.7(c), which classifies the topology of this liquid crystal texture; we shall return to this surface in a moment.

Let us compare the phenomena seen here to those in §1.2. In contrast to fluid vortices, it is experimentally possible to stabilise liquid crystal disclinations with colloids. This fact alone leads to many differences in the character of theoretical work on them. In the absence of the stabilising colloids the disclinations will shrink under effective line tension and undergo reconnections, however there is relatively little theoretical work on possible conservation laws analogous to (1.3) or on the structure of these reconnections, although some results do exist [Machon, 2017]. In this sense the dynamics of these knotted fields is less understood than is the case in fluids. It turns out, however, that there is much to be understood even about the statics of knotted liquid crystal fields. Loosely, this may be understood by observing that in a two dimensional fluid there is only one type of vortex, topologically speaking.

In a slice of liquid crystal, however, we saw there were many types, indexed by the winding of the director. What of liquid crystal textures in three dimensions? More specifically, given the knotted disclinations shown in figure 1.7, are the liquid crystal textures corresponding to them unique, or are there many inequivalent possibilities? Questions like these have a long history in liquid crystal physics which, coupled with the difference in experimental possibilities we saw above, makes some split between the character of work on knotted fields in fluids and that in liquid crystals expected.

1.3.2 Homotopy theory of knotted disclinations and Pontryagin-Thom surfaces

The traditional method of understanding liquid crystal textures containing defects is to place a measuring surface around a defect and study the possible textures on this surface, i.e. the different classes of map from the measuring surface to the space of possible values the order takes. Maps are equivalent when a continuous deformation, called a homotopy, exists between them, and as such this framework is known as the homotopy theory of defects [Mermin, 1979; Alexander et al., 2012]. For point defects in a two-dimensional slice of nematic, this is what we did above, using a circle as our measuring surface. There, the space of possible directions \mathbf{n} can point in is $S^1/\{x \sim -x\}$, the circle with antipodal points identified, also called the real projective line $\mathbb{R}P^1$. Thus the different classes of texture are reduced to the classification of maps $\mathbf{n} : S^1 \rightarrow \mathbb{R}P^1$ up to homotopy. This set of homotopy equivalence classes is denoted $[S^1, \mathbb{R}P^1]$. Actually computing this set is the work of algebraic topology [Hatcher, 2002], in which the set $[S^n, X]$ of homotopy classes of maps from a sphere S^n into a space X is termed the homotopy group $\pi_n(X)$ (group not set as the set $[S^n, X]$ is naturally given a group structure). It is found that $\pi_1(\mathbb{R}P^1) \approx \mathbb{Z}$ and thus there are infinitely many types of point defect in two dimensions as far as the traditional form of the theory is concerned; we show the four simplest in figure 1.9 but the index extends infinitely in both + and – senses. In three dimensions, the director takes values in $S^2/\{x \sim -x\}$, the sphere with antipodal points identified, also called the real projective plane $\mathbb{R}P^2$. Encircling a disclination line with a measuring loop as shown in figure 1.10, one finds $\pi_1(\mathbb{R}P^2) \approx \mathbb{Z}_2$, and thus there is exactly one type of disclination line, corresponding to the single nontrivial element of \mathbb{Z}_2 ⁶.

A limitation of this approach is that, in only considering the texture on a specific measuring surface (in practice a sphere of some dimension) it discards infor-

⁶One understands this difference by allowing the director in figure 1.9(b,e) to buckle out of the plane of the paper, reducing these textures to the trivial one. This “escape in the third dimension” causes \mathbb{Z} to undergo a mod 2 reduction.

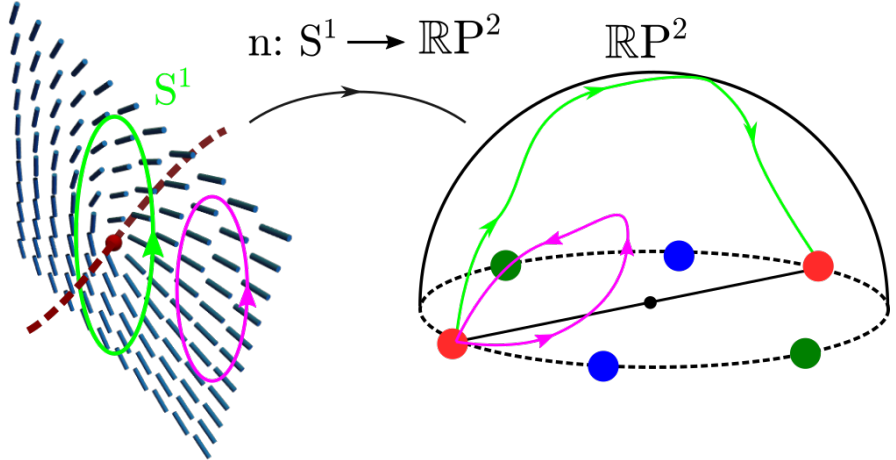


Figure 1.10: Application of the homotopy theory of defects to disclination lines. We place a measuring loop (green) around a disclination line (red curve). We then regard the director \mathbf{n} (blue cylinders) as a map from this loop to the order space of the director, in this case \mathbb{RP}^2 , modelled here as a hemisphere with equatorial points identified (pairs of red, blue, green dots indicate this identification). Homotopy theory then classifies this map as an element of $\pi_1(\mathbb{RP}^2) \approx \mathbb{Z}_2$. In this case the green curve on \mathbb{RP}^2 gives the single nontrivial element. If our measuring loop misses the disclination (purple) it traces a trivial path in \mathbb{RP}^2 .

mation about the rest of the texture, which leads to ambiguities when considering multiple defects or more complex structures such as knotted and linked disclinations [Alexander et al., 2012; Machon and Alexander, 2014, 2016a; Machon, 2016]. A more recent, global approach [Machon and Alexander, 2014, 2016a; Machon, 2016] does not fix a measuring surface, but instead classifies maps into \mathbb{RP}^2 where the domain is the entire liquid crystal sample M minus some set of (possibly knotted and linked) disclination lines L . The result is that the set of homotopy classes of the director is given by

$$[M - L, \mathbb{RP}^2] \approx H_1(\Sigma(L); \mathbb{Z}) / \{x \sim -x\}, \quad (1.6)$$

where $\Sigma(L)$ is the branched double cover of the link complement (its appearance in the result is a consequence of director non-orientability), and $H_1(\Sigma(L); \mathbb{Z})$ is its first homology group⁷. Without going into the details of this result, it is clear that these homotopy classes are far richer than the traditional classification scheme for disclinations would suggest, and that they depend strongly on the knot or link

⁷An aside: if the order space is $\mathbb{RP}^1 \approx S^1$, i.e. if one considers a phase field or a nematic confined to lie in a plane, then $[M - L, S^1] \approx H_1(M - L) \approx \mathbb{Z}$ [Lickorish, 1997]. Such vortex lines are simply classified by their winding number, with no more internal structure.

under consideration. To illustrate this point, in figure 1.11 we reproduce a ‘periodic table’ of possible textures for (p, q) torus links from Ref. [Machon, 2016]. Taking the simplest example from this table we see that for the Hopf link, consisting of two curves passing through each other once and given by $(p, q) = (2, 2)$, there are exactly two nonhomotopic textures. Returning to the knots shown in figure 1.7, for each knot there may be many nonhomotopic textures, and the knot diagram alone does not tell us which has actually been made. How should we extract this information, and visualise distinct textures? In figure 1.9 simple pictures of the director in the vicinity of a defect prove informative, but the same cannot be said of a swarm of sticks in three dimensions.

$p \setminus q$	2	3	4	5	6	7	8	9	10	11	12	13	14	15	16	17	18	19	20
2	2	3	4	5	6	7	8	9	10	11	12	13	14	15	16	17	18	19	20
3	3	2^2	3	1	\mathbb{Z}^2	1	3	2^2	3	1	\mathbb{Z}^2	1	3	2^2	3	1	\mathbb{Z}^2	1	3
4	4	3	$2 \times \mathbb{Z}^2$	5	12	7	$4 \times \mathbb{Z}^2$	9	20	11	$6 \times \mathbb{Z}^2$	13	28	15	$8 \times \mathbb{Z}^2$	17	36	19	$10 \times \mathbb{Z}^2$
5	5	1	5	2^4	5	1	5	1	\mathbb{Z}^4	1	5	1	5	2^4	5	1	5	1	\mathbb{Z}^4
6	6	\mathbb{Z}^2	12	5	$2 \times \mathbb{Z}^4$	7	24	$3 \times \mathbb{Z}^2$	30	11	$4 \times \mathbb{Z}^4$	13	42	$5 \times \mathbb{Z}^2$	48	17	$6 \times \mathbb{Z}^4$	19	60
7	7	1	7	1	7	2^6	7	1	7	1	\mathbb{Z}^6	1	7	1	7	1	7	1	7
8	8	3	$4 \times \mathbb{Z}^2$	5	24	7	$2 \times \mathbb{Z}^6$	9	40	11	$12 \times \mathbb{Z}^2$	13	56	15	$4 \times \mathbb{Z}^6$	17	72	19	$20 \times \mathbb{Z}^2$
9	9	2^2	9	1	$3 \times \mathbb{Z}^2$	1	9	2^8	1	3	\mathbb{Z}^2	1	9	2^2	1	\mathbb{Z}^8	1	9	
10	10	3	20	\mathbb{Z}^4	30	7	40	9	$2 \times \mathbb{Z}^8$	11	60	13	70	$3 \times \mathbb{Z}^4$	80	17	90	19	$4 \times \mathbb{Z}^8$
11	11	1	11	1	11	1	11	1	2^{10}	11	1	11	1	11	1	11	1	11	
12	12	\mathbb{Z}^2	$6 \times \mathbb{Z}^2$	5	$4 \times \mathbb{Z}^4$	7	$12 \times \mathbb{Z}^2$	$3 \times \mathbb{Z}^2$	60	11	$2 \times \mathbb{Z}^{10}$	13	84	$5 \times \mathbb{Z}^2$	$24 \times \mathbb{Z}^2$	17	$12 \times \mathbb{Z}^4$	19	$30 \times \mathbb{Z}^2$
13	13	1	13	1	13	1	13	1	13	1	2^{12}	13	1	13	1	13	1	13	
14	14	3	28	5	42	\mathbb{Z}^6	56	9	70	11	84	13	$2 \times \mathbb{Z}^{12}$	15	112	17	126	19	140
15	15	2^2	15	2^4	$5 \times \mathbb{Z}^2$	1	15	2^2	$3 \times \mathbb{Z}^4$	1	$5 \times \mathbb{Z}^2$	1	15	2^{14}	15	1	$5 \times \mathbb{Z}^2$	1	$3 \times \mathbb{Z}^4$
16	16	3	$8 \times \mathbb{Z}^2$	5	48	7	$4 \times \mathbb{Z}^6$	9	80	11	$24 \times \mathbb{Z}^2$	13	112	15	$2 \times \mathbb{Z}^{14}$	17	144	19	$40 \times \mathbb{Z}^2$
17	17	1	17	2	17	1	17	1	17	1	17	1	17	2^{16}	17	1	17		
18	18	\mathbb{Z}^2	36	5	$6 \times \mathbb{Z}^4$	7	72	\mathbb{Z}^8	90	11	$12 \times \mathbb{Z}^4$	13	126	$5 \times \mathbb{Z}^4$	144	17	$2 \times \mathbb{Z}^{16}$	19	180
19	19	1	19	1	19	1	19	1	19	1	19	1	19	1	19	1	2^{18}	19	
20	20	3	$10 \times \mathbb{Z}^2$	\mathbb{Z}^4	60	7	$20 \times \mathbb{Z}^2$	9	$4 \times \mathbb{Z}^8$	11	$30 \times \mathbb{Z}^2$	13	140	$3 \times \mathbb{Z}^4$	$40 \times \mathbb{Z}^2$	17	180	19	$2 \times \mathbb{Z}^{18}$

Table 2.1: $H_1(\Sigma(L))$ for (p, q) torus links with $2 \leq (p, q) \leq 20$. x implies a group \mathbb{Z}_x , integer summands are given as usual.

Figure 1.11: A ‘periodic table’ of homotopy classes of nematic textures for (p, q) torus links. Note the diversity: the sets may be finite or infinite, the number of \mathbb{Z} components varies, and the number of elements in the finite component of each set may vary dramatically.

One solution is a construction which generalises the dark brushes of schlieren textures to three dimensions — the Pontryagin-Thom construction [Chen, 2012; Chen et al., 2013; Machon, 2016; Alexander, 2018]. The idea is to extract the set of all points in the liquid crystal domain where the director lies in the horizontal plane — more precisely, perpendicular to some fixed direction in $\mathbb{R}P^2$ which we call the vertical axis. This is exactly what a schlieren textures shows in a two dimensional slice using $\mathbb{R}P^1$ instead, although schlieren textures contain some redundancy, showing us the set where the director is along some direction (V in figure 1.9(a), say) and also perpendicular to that direction (H in figure 1.9(a), the analogy to the horizontal plane in a three-dimensional texture) — we only really need half this data. In a three dimensional sample this ‘horizontal set’ is not comprised of lines as in the two-dimensional schlieren texture but is a surface, the Pontryagin-Thom (PT) surface. After finding this surface, the construction is completed by

colouring it according to the orientation in the horizontal plane that the director takes. An illustration of this procedure is shown in figure 1.12(a). A powerful result in Algebraic Topology called the Pontryagin-Thom correspondence [Milnor, 1997; Hatcher, 2002] shows that these coloured surfaces, taken up to smooth deformations (more precisely framed cobordisms), are in one-to-one correspondence with homotopy classes of maps, and so textures may be visually distinguished by their differing PT surfaces. To illustrate this fact, in figure 1.12(b) we show the two distinct PT surfaces for the two nonhomotopic Hopf link textures [Machon, 2016] (that they are both a single colour is an indication that representatives from both homotopy classes can be chosen with the director everywhere in the domain perpendicular to some axis, in particular one of the two horizontal axes). Returning to figure 1.7(c), this construction provides the coloured surfaces shown; by examining the surface and the colour windings upon it, we may place the texture in one of the classes from (1.6). PT surfaces represent an enormous compression of information into a visually immediate form, and their utility is far from limited to disclination lines; we shall use them in our own work in §??.

Now that we have seen some of the theoretical developments in knotted liquid crystals — the homotopy classification, the Pontryagin-Thom construction — let us remark again on the similarities and differences to fluids. Topological invariants play a vital role in both, linking and self-linking in fluids and homology groups of the link complement in liquid crystals. Indeed, the self-linking of liquid crystal textures will give rise to inequivalent colour windings on their PT surface and differing elements of the homotopy classification. However in contrast to fluids, where knot reconnections have been experimentally tracked and studied, there has been almost no mention of dynamics and link reconnections. When this happens, the topology of the link complement changes, and point defects may even be nucleated, perhaps a daunting theoretical task given that existing theory primarily assumes the domain is fixed, and even then finds a richness of possibility. We shall not develop this line of questioning further here, but invite the reader to consult Ref. [Machon, 2017] for theoretical developments in this direction. In summary, we simply remark that it is increasingly clear the world of knotted fields is far broader than fluids.

1.3.3 Beyond disclination lines

The above sections focused on the knotting and nontrivial topology of disclination lines — defects in the director \mathbf{n} itself. Given the experimental focus on systems of this kind, and their direct connection to the idea of a knotted field, this is natural. However even in the absence of defects liquid crystals support an array of topolog-

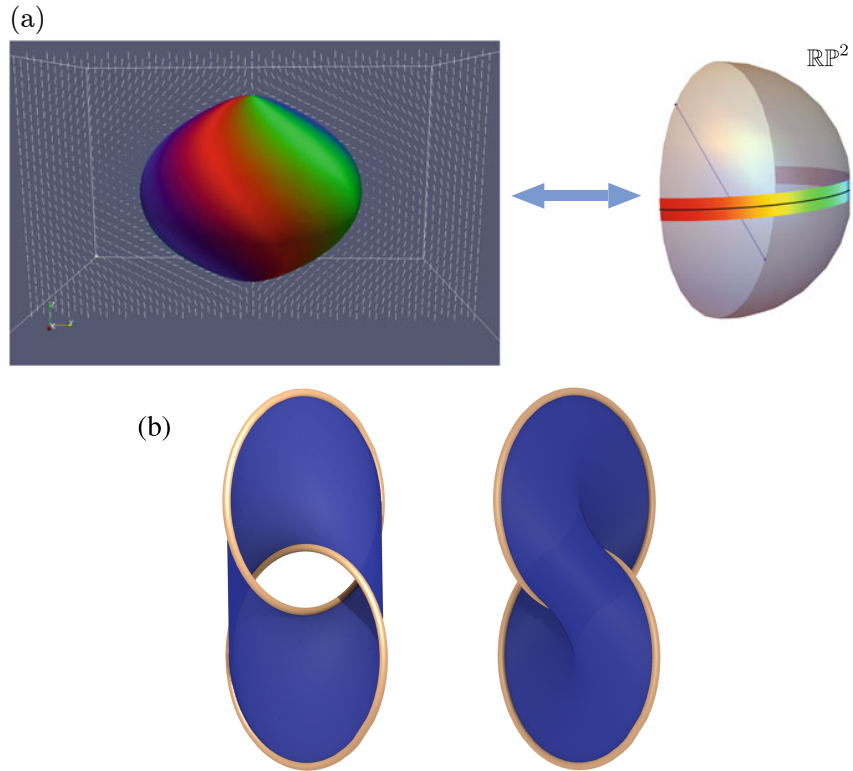


Figure 1.12: (a) The Pontryagin-Thom construction. The set where the director is horizontal is extracted and coloured by the angle the director makes in the horizontal plane (coloured band on \mathbb{RP}^2 with corresponding colours in the domain). Note that in contrast to the more standard picture of \mathbb{RP}^2 shown in figure 1.9 here it is ‘turned on its side’ so that, visually, the horizontal plane through it (which one should imagine as also being the horizontal plane in the liquid crystal domain), does not coincide with the boundary of the hemisphere. The texture shown here is a topologically nontrivial one called a toron [Smalyukh et al., 2010], containing two strength 1 point defects at its top and bottom, each detected by two rotations of the colour wheel on the PT surface. (b) Two distinct (noncobordant) PT surfaces for the Hopf link, representing the two possible nonhomotopic textures of figure 1.11. Figures reproduced from Ref. [Alexander, 2018; Machon, 2016].

ical phenomena which may also be considered examples of knotted fields, although perhaps in a different sense to those discussed above.

Skyrmions and Hopfions

The most well known topological feature of this kind is a skyrmion, an example of which is shown in figure 1.13(a) given by the vector field $\mathbf{n}(r) = \cos(\pi r)\mathbf{e}_z + \sin(\pi r)\mathbf{e}_r$ on the unit disk. Fixing the director on the disk boundary, we may wrap this texture around a sphere (compactifying the boundary to a point) at which point its topology is captured by a map $\mathbf{n} : S^2 \rightarrow S^2$, in other words an element of $\pi_2(S^2) \approx \mathbb{Z}$. These textures are a well studied feature of vector and line fields in two dimensions [Alexander, 2018]. We are primarily interested in the properties of order in three dimensions, and as such focus on their three dimensional ‘cousins’: Hopfions. An experimental image of a Hopfion is shown in figure 1.13(b)[Chen, 2012; Chen et al., 2013]. The figure shows a nematic liquid crystal texture inside a three dimensional cell, where the PT surface has been constructed by extracting director orientation via three-photon fluorescence microscopy. What qualifies the Hopfion as a knotted field becomes clear on viewing this surface: each stripe of colour twists about a torus, linking each other colour exactly once — in a Hopf link, no less. Skyrmions are classified by an element of $\pi_2(S^2)$. Hopfions are instead classified by $\pi_3(S^2)$, the third homotopy group of the sphere. Heinz Hopf famously showed that $\pi_3(S^2) \approx \mathbb{Z}$, and in doing so constructed an explicit example of a nontrivial element of this group — the celebrated Hopf fibration. For mathematical detail on the construction of the fibration we refer to the reader to Refs. [Bott and Tu, 1982; Alexander, 2018], and for an excellent video of its structure we urge the reader to consult Ref. [Johnson, 2011]. What figure 1.13(b) shows is an experimental image of this fibration; the energetics of the liquid system favour a fixed far field nematic direction, mimicking the skyrmion boundary conditions and allowing the domain to be compactified from \mathbb{R}^3 to $\mathbb{R}^3 \cup \text{pt} \approx S^3$. The nematic texture then realises a map $\mathbf{n} : S^3 \rightarrow \mathbb{RP}^2$, and $\pi_3(\mathbb{RP}^2) \approx \pi_3(S^2) \approx \mathbb{Z}$. The fact that the order lies in \mathbb{RP}^2 not S^2 is reflected in that fact that there are two stripes of each colour on the experimental fibration [Chen et al., 2013; Ackerman and Smalyukh, 2017]; in figures 1.13(c)–(d) we show a Hopfion in vector order, containing only single stripes, with two particular stripes picked out to make the linking clear.

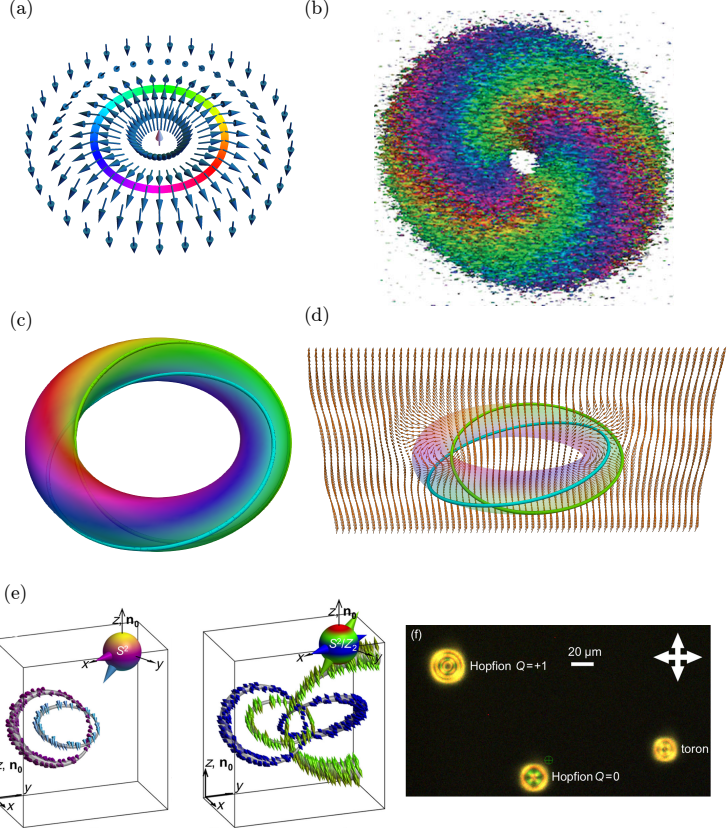


Figure 1.13: Defect free, topologically nontrivial textures. (a) A skyrmion given by $\mathbf{n}(r) = \cos(\pi r) \mathbf{e}_z + \sin(\pi r) \mathbf{e}_r$, classified by an element of $\pi_2(S^2) \approx \mathbb{Z}$, here +1. One way to visualise this is by plotting the PT surface for the skyrmion and noting its +1 winding. (b) An experimental image of a Hopfion in nematic order, with reconstructed PT surface. It is classified by an element of $\pi_3(\mathbb{R}P^2) \approx \mathbb{Z}$, here +1, which may be computed via the linking number of the different stripes of colour. That there are two stripes of each colour reflects that fact that the order space is $\mathbb{R}P^2$ not S^2 (see the following panels). (c,d) A simulation of of Hopfion in vector order (order space S^2), with stripes of two colours picked out to aid visualisation of their linking. Note that in vector order there is only a single stripe of each colour. (d) shows a cross section of the director field corresponding to this Hopfion. (e) Recent experimental image of a Hopfion, clearly showing the telltale linking of preimages. The first panel shows a vectorised director, i.e. a choice of arrowhead has been made. In the second panel, it has not, and linking of two colours for antipodal vectors becomes linking of the same colour. (f) Polarising optical micrograph of Hopfions and other textures. Arrows showed crossed polariser directions, and the green circled cross denotes the size of the laser tweezer which manipulates them. Panels (b,e,f) reproduced from Ref. [Chen et al., 2013; Ackerman and Smalyukh, 2017].

The geometry of vector fields

The linking of inverse images is the hallmark of the Hopf texture (figure 1.13(e)). However without data processing this linking is not an immediately apparent feature of the director. By contrast the knotted disclinations, and even their associated PT surface, in figure 1.7 may be clearly visualised. This is a consequence of the coupling of these topological features to the geometry, energetics and ultimately interaction with light of the liquid crystal, a coupling not present in the inverse images characterising the Hopfion in figure 1.13(e). This observation invites the question: are there ‘natural’ features of the Hopfion, or nonsingular liquid crystal textures in general, which can be used to infer their topology? We will explore this question, with a particular focus on a recently discovered phase of liquid crystal [Jákli et al., 2018], in §???. The focus will be on naturally geometric structures inside the liquid crystal which also contain some topological information, and so we now discuss the geometry of liquid crystals, and vector fields more generally.

The fundamental geometry and energetics of nematics was encoded by Frank in 1958 [Frank, 1958], where he gave a free energy for their elastic distortions. We give this free energy here in a slightly nonstandard form, following Refs. [Machon, 2016; Selinger, 2019]:

$$F = \int d^3\mathbf{r} \quad \frac{K_1}{2}(\nabla \cdot \mathbf{n})^2 + \frac{K_2}{2}(\mathbf{n} \cdot \nabla \times \mathbf{n})^2 + \frac{K_3}{2}((\mathbf{n} \cdot \nabla)\mathbf{n})^2 + \frac{K_{24}}{2}\text{Tr}(\Delta)^2, \quad (1.7)$$

where the various K_i are elastic constants⁸. Each term in (1.7) comes from a different mode of distortion for the liquid crystal, shown in figure 1.14:

$$(\mathbf{n} \cdot \nabla)\mathbf{n} \quad \text{Bend}, \quad (1.8)$$

$$\mathbf{n} \cdot \nabla \times \mathbf{n} \quad \text{Twist}, \quad (1.9)$$

$$\nabla \cdot \mathbf{n} \quad \text{Uniaxial splay}, \quad (1.10)$$

$$\Delta(\bullet) := \frac{1}{2} \left((\bullet \cdot \nabla \mathbf{n}) + \mathbf{n} \times (\mathbf{n} \times \bullet \cdot \mathbf{n}) \right) \quad \text{Biaxial splay}. \quad (1.11)$$

Vector order has a local rotational symmetry under which the free energy (1.7) must remain invariant, and indeed the above terms are exactly those combinations of gradients which respect this symmetry. More precisely, the terms appearing in (1.7) correspond to the magnitudes of the irreducible representations of $\nabla \mathbf{n}$ under the action of the rotation group $SO(2)$. These piece together to give a decomposition of $\nabla \mathbf{n}$ which is naturally written in terms of gradients parallel and perpendicular to

⁸These constants do not match one-to-one with those found in the standard writing of the Frank free energy; see Ref. [Selinger, 2019].

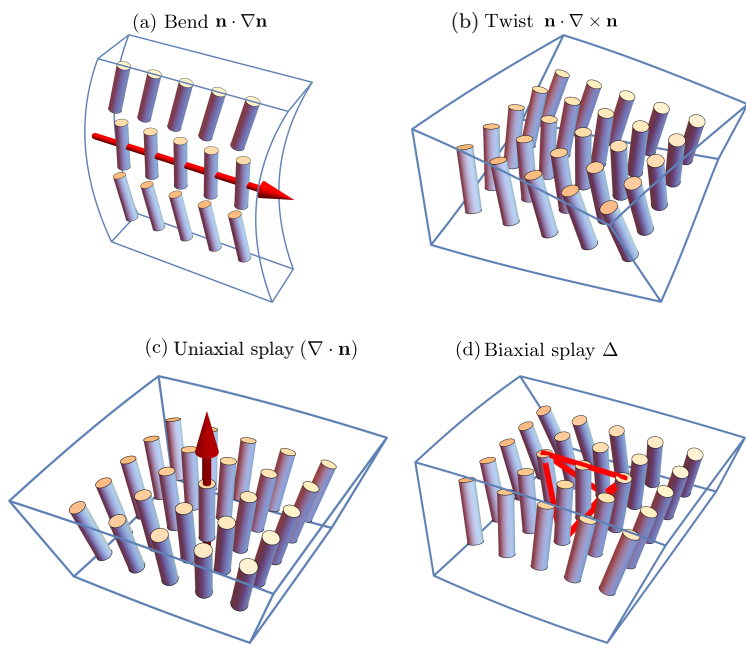


Figure 1.14: The four modes of director deformation: Bend, twist, (uniaxial) splay and biaxial splay. The vector plotted in (c) is the splay vector $(\nabla \cdot \mathbf{n})\mathbf{n}$. Biaxial deformations, described by a rank two tensor (not a vector as in (a),(c)) are represented by a tetrahedron corresponding to the triple $\{\mathbf{n}, \Delta_1, \Delta_2\}$, where Δ_i denotes the i th eigenvector of Δ . Figures reproduced from Ref. [Selinger, 2019].

the director, $\nabla \mathbf{n} = \nabla_{\parallel} \mathbf{n} + \nabla_{\perp} \mathbf{n}$, where

$$\nabla_{\parallel} \mathbf{n} = \mathbf{n}^* \otimes (\mathbf{n} \cdot \nabla) \mathbf{n}, \quad (1.12)$$

$$\nabla_{\perp} \mathbf{n} = \frac{\nabla \cdot \mathbf{n}}{2} I_{\perp} - \frac{\mathbf{n} \cdot \nabla \times \mathbf{n}}{2} J + \Delta. \quad (1.13)$$

I_{\perp} is the identity transformation after restriction to perpendicular directions, and $J = \mathbf{n} \times \bullet$ is rotation about \mathbf{n} ⁹. The geometry of $\nabla_{\perp} \mathbf{n}$ and Δ in particular has been explored in Ref. [Machon and Alexander, 2016b]. $\nabla_{\perp} \mathbf{n}$ describes how \mathbf{n} varies as one moves in a plane perpendicular to it; this is a classical object in the differential geometry of surfaces called the shape operator. The decomposition (1.13) corresponds to its breakdown into an isotropic piece I_{\perp} , an antisymmetric piece J and a traceless symmetric piece Δ (if \mathbf{n} were the normal to a family of surfaces the antisymmetric piece would vanish). All directional information is contained in Δ ; its eigenvectors coincide with those of $\nabla_{\perp} \mathbf{n}$ and pick out the two directions of principal curvature in the plane perpendicular the director, explaining the name “biaxial splay” for its mode of distortion. The geometry of $\nabla_{\parallel} \mathbf{n}$ is less well explored. It describes the bending of the director field: if one traces a single curve to which \mathbf{n} is tangent, then $\nabla_{\parallel} \mathbf{n}$ gives the classical curvature from the differential geometry of space curves [DoCarmo, 1976]. A more complete account of its geometry will, in part, be the topic §??.

Each of the pieces in (1.12), (1.13) is manifestly geometric, but they also represent topological information, as canonical sections of vector bundles defined by the director. At each point in the material, the director \mathbf{n} splits the tangent space into a line parallel to \mathbf{n} , L_n , and a plane perpendicular to it, ξ , $T\mathbb{R}^3 \approx L_n \oplus \xi$. An example of this splitting for a skyrmion texture is shown in figure 1.15. The families of lines L_n and planes ξ vary smoothly with the director, and such smoothly varying families of vector spaces are called vector bundles [Tu, 2010; Milnor and Stasheff, 1974]. The most famous example of a vector bundle, and the interesting properties they can have, is the family of planes tangent to S^2 (its tangent bundle). The Poincare-Hopf theorem tells us one cannot ‘comb a sphere’ [Milnor, 1997], in other words one cannot choose a nonzero tangent vector everywhere on the sphere. Said more technically, one cannot find an everywhere nonzero section of the tangent bundle to the sphere. This failure is connected to the topology of S^2 ; if one sums the windings of all the zeros in an attempted vector field one obtains the Euler

⁹That the splay term appears squared in (1.7) is because the decomposition (1.12),(1.13) is for vector order, not nematic order. The additional symmetry $\mathbf{n} \sim -\mathbf{n}$ forces us to square this term. That the twist term is squared is because nematics are achiral. In a cholesteric liquid crystal [Beller et al., 2014] one has $(\mathbf{n} \cdot \nabla \times \mathbf{n} + q_0)^2$, giving a linear term on expansion of the square.

characteristic of S^2 . An entirely analogous result holds for any vector bundle; the zeros of a section of a vector bundle encode its Euler class [Bott and Tu, 1982; Milnor and Stasheff, 1974]. Returning to (1.12), (1.13), $\nabla_{\perp} \mathbf{n}$ is a section of the bundle $\xi^* \otimes \xi$ — it maps vectors orthogonal to \mathbf{n} into vectors orthogonal to \mathbf{n} — and the bend $\nabla_{\parallel} \mathbf{n}$ is a section of the bundle $L_n^* \otimes \xi$. Both probe the topology of ξ and, loosely speaking, as ξ is in one-to-one correspondence with the director \mathbf{n} this topology carries over to \mathbf{n} . The zeros of Δ , called umbilic lines in analogy to the umbilic points of the differential geometry of surfaces, have been investigated in Ref. [Machon and Alexander, 2016b]. The zeros of $\nabla_{\parallel} \mathbf{n}$, which we will call β lines, will be the subject of §??.

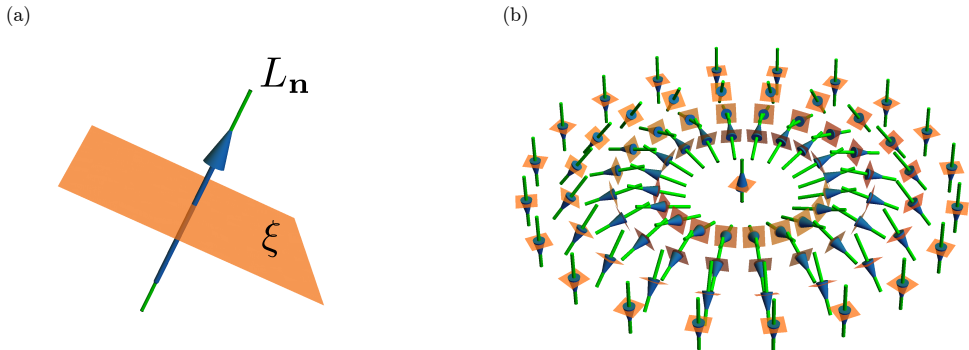


Figure 1.15: The director \mathbf{n} splits space into families of lines L_n parallel to it, and a family of planes ξ perpendicular to it: $T\mathbb{R}^3 \approx L_n \oplus \xi$. Panel (a) shows this splitting at one point, with the director a blue arrow, L_n the green line and ξ the orange plane. This splitting is shown for an entire skyrmion texture in panel (b). Compactifying the boundary of this skyrmion, i.e. considering the outer ring of vectors and planes to really only be one vector and one plane, the skyrmion texture is topologically the family of normal vectors to S^2 , and ξ is its tangent bundle. As such, a smoothly varying choice of vectors tangent to the family of planes ξ (section of the bundle) cannot be made (it is worth imagining trying to do so: make some choice of the same fixed vector for all the outer ring of planes, and then try and extend inwards. This amounts to combing one half of the sphere and finding one cannot also comb the other).

The umbilic and β lines are natural geometric structures found in any vector field. However, they assume a particular relevance when strongly coupled to the energetics of the liquid crystal texture. One way to do this is to frustrate the liquid crystal with boundary conditions, as in the disclinations of figure 1.7. Another is to pass to a different phase of liquid crystal, where such coupling exists. In the case of

umbilic lines, this setting is the cholesteric phase [Beller et al., 2014], in which the liquid crystal has a preference for nonzero twist; Δ turns out to be related to the axis of this twisting [Alexander, 2018], and its zeros thus encode energetic frustration inside the cholesteric [Machon and Alexander, 2016b]. For β lines, the natural setting is a recently discovered phase of liquid crystal, the twist-bend or splay-bend nematic [Jákli et al., 2018]. These materials, comprised of banana shaped molecules, have an energetic preference for everywhere nonzero bend. A second focus of §?? will be on this interplay between geometry and energetics in twist-bend nematics.

1.4 Modern knotted fields: excitable media

“In excitable media we may have a new context in which something like a vortex atom theory can live again, strangely transfigured.”

A. T. Winfree, The Geometry of Biological Time, Chapter 9.

We now come to our final example of knotted fields, those found in excitable media. We might have discussed them immediately after fluids and superfluids, and indeed we will see closer similarities to those systems than to liquid crystals. That we chose not to is a reflection of their relative lack of experimental development. By way of prelude, the modern state of affairs in these systems is that the analogy to a fluid vortex ring can be generated experimentally [Bánsági and Steinbock, 2006; Azhand et al., 2014; Totz et al., 2015]. Figure 1.16 shows a schematic of a thick dish of the Belousov-Zhabotinsky (BZ) reagent, a medium which supports waves of propagating chemical activity. Axially symmetric waves of such activity spiral outwards from a ‘singular’ ring shown in red — exactly what is occurring on this ring will be discussed below. Beneath it is an experimental realisation of this setup from Ref. [Totz et al., 2015], viewed from the side in figures 1.16(a)–(e) and from the top in figures 1.16(f)–(g). From the side the ring appears as a discontinuity in the emitted wavefronts, with a second such discontinuity where the fronts collide in the middle of the dish. Figures 1.16(a)–(e) show stacks of snapshots of different rings evolving over time, with the overlaid red curves tracking their position. They show, firstly, that the rings stably persist over several hours, and secondly that they have their own dynamics, expanding, contracting or reaching a stable radius (the outcome may be experimentally tuned). The topological possibilities, dynamics, and organisation of the entire excitable medium by these rings are the subject of this section, and of §??. These rings have not yet been experimentally tied in nontrivial configurations — as we shall see in this section, such an experiment would be extremely interesting.

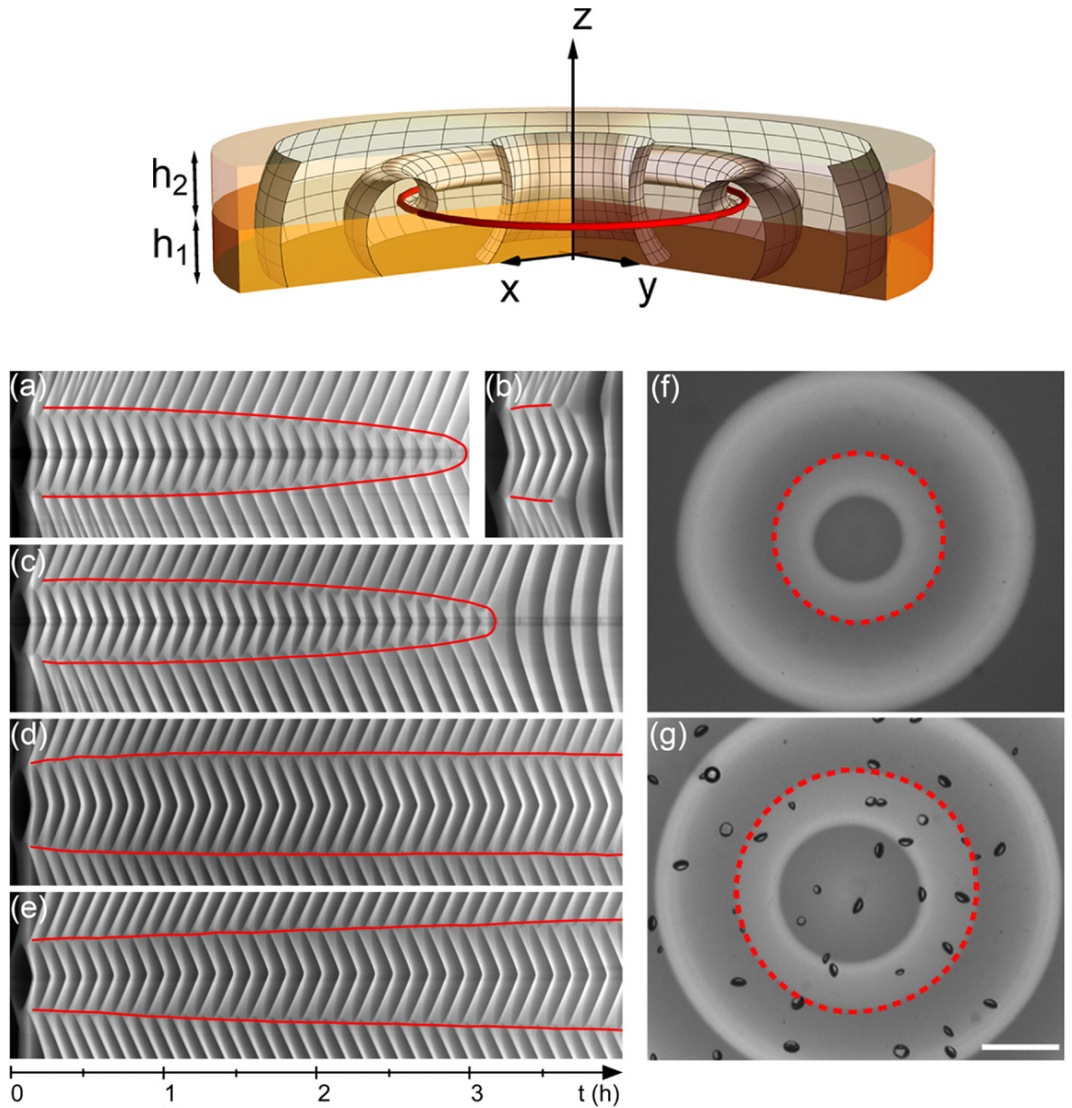


Figure 1.16: Top Panel: Schematic illustration of a vortex ring in excitable media. A dish of the Belousov-Zhabotinsky reagent supports an axially symmetric spiralling wave of chemical activity (meshed wavefronts) emanating from a ring shaped singularity shown in red. Bottom Panel: An experiment realising this setup. (a)–(e) shows a time series of the dish viewed side on, i.e. the x - z plane, over 4 hours. The rotation period of the wave itself is $390\text{s} \approx 6\text{--}7\text{ mins}$. In each frame, the ring appears as a pair of points with wavefronts emanating from it, which collide in the middle of the dish. Over time the ring moves, tracing the curves shown. Depending on the heights h_1 and h_2 it may shrink (a), (c), reach a steady radius (d) or expand (e). (f) and (g) show the ring from above (x - y plane) over 3 hours. Setting spatial scale, the white bar in (g) corresponds to 5 mm. Figures reproduced from Ref. [Totz et al., 2015].

Excitable media

The building block of an excitable medium is an excitable oscillator, something which rests in a quiescent locally stable state but which, given a small kick, becomes excited before relaxing back to quiescence. A prototypical example is a nerve cell. Given an electrical input, the cell ‘fires’, becoming excited, before slowly relaxing back to its resting state where it can be triggered again. An excitable medium is a continuum of these oscillators, all coupled together, in our case by diffusion of activity from one oscillator to its spatial neighbours. Such media support waves of activity, where an excitation in one oscillator triggers its neighbours to ‘fire’ also. A pleasing example of such waves is a grass fire [Winfree and Strogatz, 1983a]. The oscillators are blades of grass. Their resting state is unburnt, their excited state burnt. After burning, the blades slowly grow back, able to be burnt again. A field of grass, the excitable medium, supports a wave of excitation, i.e. a moving front of grass fire. Note the front has a leading edge (the transition from unexcited to excited) and a trailing edge (the transition from excited to unexcited).

There is an enormous experimental and theoretical literature on systems exhibiting this sort of behaviour; for references see [Winfree, 2001]. We present a minimal mathematical model, which shall be the focus of §??, and which provides an effective description of many more complex excitable media [Winfree, 2001]: the FitzHugh-Nagumo model [FitzHugh, 1961; Nagumo et al., 1962]

$$\frac{\partial u}{\partial t} = \frac{1}{\epsilon}(u - \frac{1}{3}u^3 - v) + \nabla^2 u, \quad (1.14)$$

$$\frac{\partial v}{\partial t} = \epsilon(u + \beta - \gamma v). \quad (1.15)$$

Here $u(\mathbf{x}, t)$, $v(\mathbf{x}, t)$ are two real valued scalar fields, with ϵ, γ, β model parameters. The coupling which turns this system from an excitable oscillator to an excitable medium is through diffusion $\nabla^2 u$, in this instance in the u variable only (although variants with diffusion in each variable also exist). The phase plane for the differential equation system without diffusion is shown in figure 1.17(a), with parameter choices which will generate an excitable oscillator. The system has a fixed point (u^*, v^*) (black dot), but given a finite perturbation in u it will execute a large loop in phase space called the excitation-recovery loop, jumping to the upper branch of the u nullcline, crawling along it until the first inflection, whereupon it jumps to the lower branch and crawls again back to the fixed point (black arrows in the figure). In the sense that a perturbation in u instigates this loop, u might be considered an ‘excitor’ variable and v a ‘recovery’ variable.

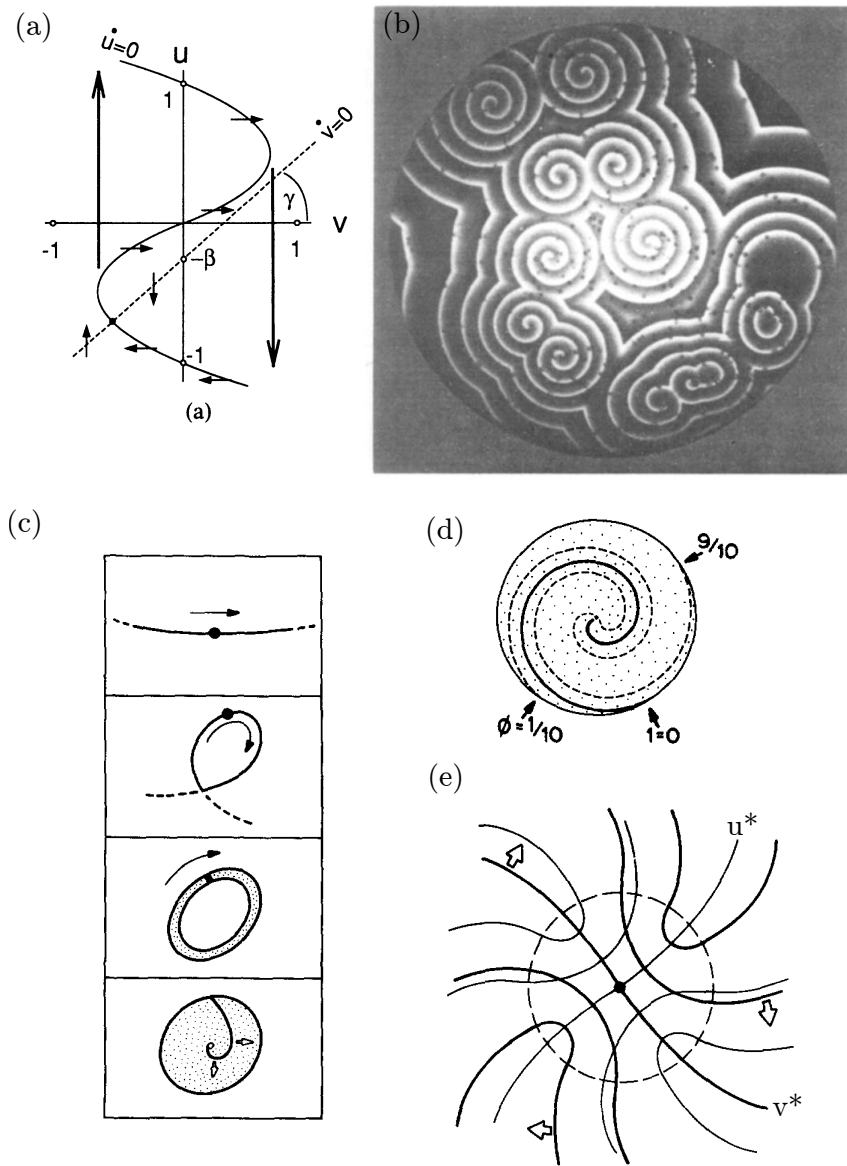


Figure 1.17: Spiral waves in two dimensions. (a) The phase plane of the FitzHugh-Nagumo model (1.15), with u and v nullclines (solid and dotted curves), fixed point (black dot) and excitation-recovery loop (large black arrows) shown. This loop is topologically a circle S^1 , and progression through a cycle of excitation-recovery can be described by a phase $\phi \in S^1$. (b) Spiral waves in a dish of the BZ reagent. (c) –(e) The anatomy of a single spiral wave. In (c) one imagines setting a pulse of excitation running around a closed loop, which gradually thickens until the propagation time around its inner edge is faster than the medium can recover from. The resulting structure is a spiral wave. (d) shows its phase description, with three example isophase spirals shown. (e) A qualitative picture of the (u, v) field around a spiral wave vortex. Away from the vortex the contours are parallel, but inside they necessarily cross one another transversally. Figures reproduced from Ref. [Winfree and Strogatz, 1983a].

The topological possibilities of excitable media

The key topological observation is that the excitation-recovery loop is a circle S^1 . In a portion of excitable media M , the state of a typical point lies somewhere on this loop, and thus we can describe the system with a map $\phi : M \rightarrow S^1$, a situation encountered before in superfluids. Concretely mapping between (u, v) and ϕ may be achieved via something of the form $(u, v) = (2 \cos \phi - u^*, \sin \phi - v^*)$, stretching S^1 over the excitation-recovery loop. That the system is characterised by the phase field $\phi \in S^1$ immediately implies the potential existence of knotted and linked vortices if our domain M is three-dimensional, again by simple analogy with superfluids. What makes this system so interesting is that the character and dynamics of these phase singularities are very different to what we have encountered before.

In two dimensions these singularities are at the core of spiral waves, a collection of which are shown in the BZ reagent in figure 1.17(b). The anatomy of a single spiral wave is dissected in figure 1.17(c)–(e). In figure 1.17(c), one imagines taking an initially thin ring of excitable medium and setting a wave of excitation running around it. If the ring is thickened, we expect some spatial variation in the wavefront—it turns out that given isotropic diffusion in (1.15) it takes the shape of an involute spiral started from the inner edge of the ring [Winfree, 2001]. This thickening process happily continues until the time taken for the inner edge of the wave to circulate once is comparable to the recovery time of the medium, a condition which defines a ‘core region’, inside of which the (u, v) states of points leave the excitation-recovery loop and so cannot be reliably assigned a phase ϕ (this is analogous to what happens inside the healing lengthscale which sets vortex core size in superfluids). A phase description in which the core is idealised to zero radius is shown in figure 1.17(d), and a qualitative picture of the corresponding contours of (u, v) is shown in figure 1.17(e). These ‘rotors’ periodically emanate waves of excitation which organise the entire medium, splitting it into domains separated by shock structures where two wavefronts coincide and annihilate (figure 1.17(b)).

In three dimensions, we have a linelike phase singularity, a vortex filament, emitting ‘scroll waves’. The geometric and topological possibilities of linked and knotted vortex filaments were first investigated in a series of papers by A.T. Winfree and S. Strogatz [Winfree and Strogatz, 1983a,b,c, 1984]. The simplest possibility is for the filament to close into a ring, emitting axially symmetric waves which fill space as shown in figure 1.18(a). This is the situation encountered experimentally in figure 1.16. However, Winfree and Strogatz demonstrated numerous other possibilities. For example, we once again have internal structure along the singularity, in this case the angle the $\phi = 0$ contour (say) makes with the filament in successive

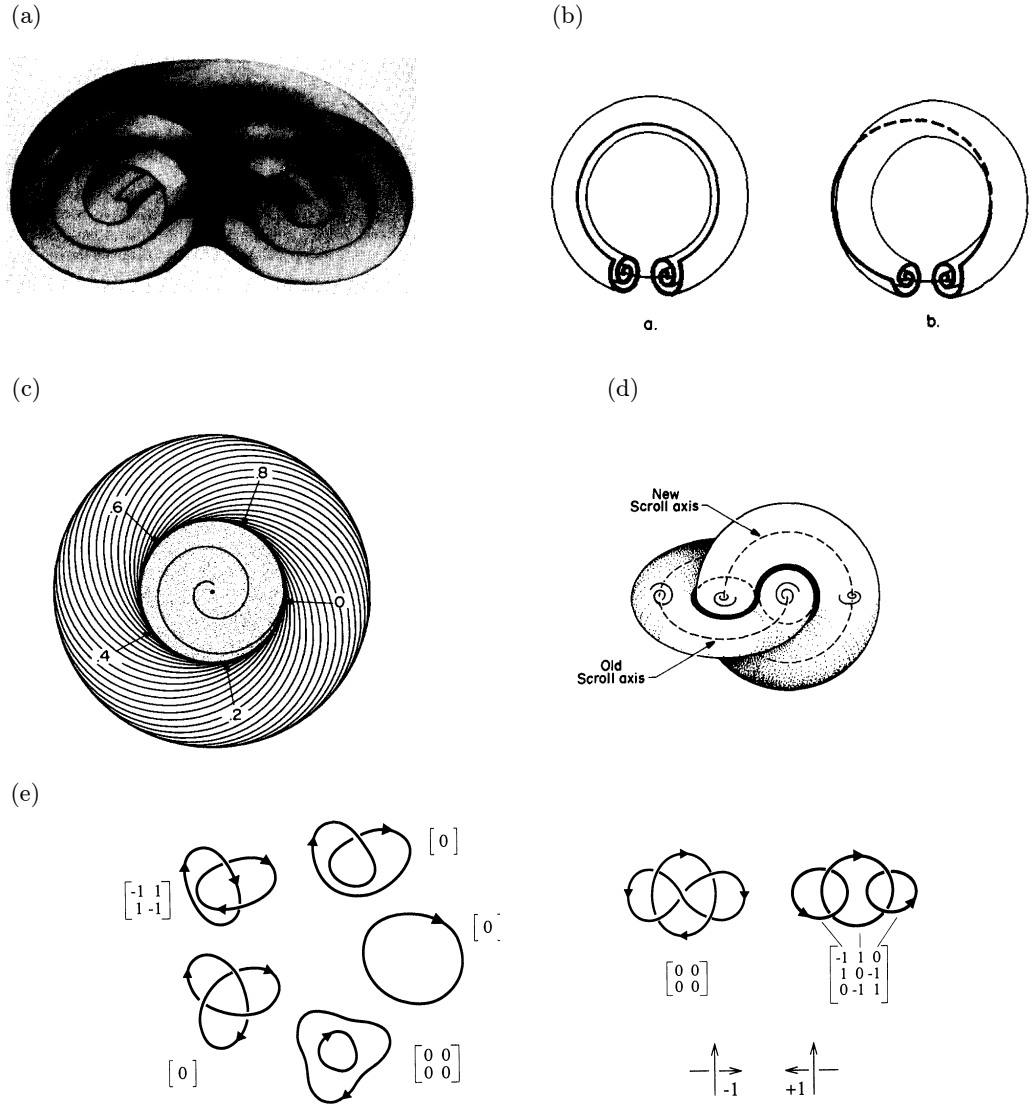


Figure 1.18: The topological possibilities of knotted vortices in excitable media. (a) A spiral wave rotated around an axis of symmetry forms a scroll wave, shown in cross section with wavefronts in grey. This is the system realised in figure 1.16. (b) Cutting a scroll wave, putting a full turn of each phase contour into it, then gluing back together. (c,d) This twisted scroll ring has a full cycle of phase around its equator (points 0 through 8 in panel (c)), necessitating the existence of a second twisted scroll ring linking the first, shown in (d). (e) Two groups of knotted vortices, with transmutations topologically allowed between neighbouring elements of each group. The matrices shown have (i, j) th element $Lk(C_i, C_j)$, where $Lk(C_i, C_i) := SL(C_i)$. Note each row (and column) sums to zero, an expression of (1.16). Figures reproduced from Refs. [Winfree and Strogatz, 1983a,b; Winfree, 1990].

cross sections along it, which opens up the possibility of self-linking. The simplest such scenario, a twisted scroll wave, is shown in figures 1.18(b)–(c). Focusing on figure 1.18(c), we note that such twisting implies a full cycle of phase about a line threading the hole in the ring. In other words, a second phase singularity must exist along this line too! Closing this line into a second loop, we obtain figure 1.18(d); two scroll rings, each with linking and self-linking number (+)1. Winfree and Strogatz extend this line of reasoning in a manner similar to that of Moffatt in Ref. [Moffatt, 1969] to derive a topological selection rule on allowed configurations of knotted vortices:

$$0 = \sum_{i,j, i \neq j} Lk(C_i, C_j) + SL(C_i), \quad \forall i. \quad (1.16)$$

This rule has a similar feel to the helicity count of (1.3), but its content is slightly different. It is a condition each knotted loop in a link must satisfy in order for the whole to exist. In fact a separate continuum definition of a helicity has been given [Trueba and Arrayás, 2009] but it is currently not clear (to me at least) how the concepts interlink; it is an interesting question for further study ¹⁰.

The dynamical possibilities of excitable media

Provided the topological constraint (1.16) remains satisfied, there is no reason link reconnections cannot occur, as they do in the other systems we have discussed. In figure 1.18(e) we show two groups of allowed knotted vortices, and within each group transmutations are topologically allowed. As Winfree and Strogatz note, questions of whether or not they actually occur in a given excitable medium “probably depend sensitively on the exact kinetics of the medium” [Winfree and Strogatz, 1984]. In the experiment of figure 1.16 [Totz et al., 2015] we saw that these vortex lines are not merely static emitters of wavefronts, they have their own dynamics, and one has no *a priori* reason to expect these dynamics to preserve topology. What is absolutely remarkable is that, in a certain parameter regime in the FitzHugh-Nagumo model, it was found that they do [Winfree, 1990; Henze, 1993]. Using $\epsilon = 0.3, \beta = 0.7, \gamma = 0.5$, a stable vortex ring was found in [Courtemanche et al., 1990], shown in figure 1.19(a), followed by a stable trefoil knot [Henze and Winfree, 1991](in a slightly different kinetics) and then a variety of apparently stable knots and links [Henze, 1993] summarised in figure 1.19(b). An account of this first period of development may be found in Refs. [Winfree, 1990, 2001, 2002]. Subsequent work [Sutcliffe and Winfree, 2003] confirmed a wide basin of stability for the trefoil knot

¹⁰ (1.16) corresponds to giving the link its Seifert framing [Winfree and Strogatz, 1983c; ed. H. K. Moffatt ed., 1992], already seen in superfluids in footnote 3, for which $\mathcal{H} = 0$.

and the Hopf link over substantially larger time periods than the original trefoil simulations were run for. More recently, Maucher and Sutcliffe [Maucher and Sutcliffe, 2016] showed that the FitzHugh-Nagumo dynamics is even capable of simplifying a tangled unknot into a unique canonical round form, as well as demonstrating stable forms for more complex knots — the figure-eight and torus links in certain geometries [Maucher and Sutcliffe, 2017]. A simplification of an unknot with 13 crossings in projection is shown in figure 1.19(c), with a cross section to show the associated wavefield in figure 1.19(d) (one might compare to figure 1.17(b)). The stable torus and figure-eight knots with associated minimal lengths are shown in figure 1.19(e). These numerical findings are in stark contrast to what we saw in fluids, superfluids and liquid crystals (indeed, in most knotted fields), and invite a series of questions: What determines the dynamics of these vortices? How are reconnections avoided? What is the mechanism of knot untangling? Are all knots stable, and if so can we predict their shapes? In some form these questions have existed since the first knotted vortices were discovered. Initial theoretical work focused heavily on the idea that their laws of motion could be explained by a ‘local geometry hypothesis’ [Keener, 1988; Keener and Tyson, 1992; Biktashev et al., 1994; Henry and Hakim, 2002; Echebarria et al., 2006; Dierckx, 2010] in which dynamics at each point on the curve were governed by some local law of motion involving its curvature, the twist of spiral wave phase etc. After a perturbative theory for such a law was developed [Keener, 1988; Keener and Tyson, 1992; Biktashev et al., 1994], substantial work went into testing whether or not this was the case [Winfree, 1990; Henze, 1993], of which an account may be found in [Winfree, 2002]. Summarising very coarsely, such laws found some success in describing isolated filaments, but of course encounter problems whenever interfilament interactions are required. The problem is that evidence ultimately suggested such interactions were integral to describing stable knots [Henze, 1993; Winfree, 2002], and as such a local geometry hypothesis failed to account for their dynamics. The observed untangling without reconnection of unknots shown in figure 1.19(e) [Maucher and Sutcliffe, 2016] further casts doubt on whether such a law could be made to work.

We remark that the idea of reducing the dynamics of an entire field to that of a curve is not unique to excitable media, but cuts across knotted fields. In particular the idea is similar to the Local Induction Approximation (LIA) in fluids and superfluids [Saffman, 1992], in which the Biot-Savart law of motion governing vortex lines is approximated by a dominant contribution arising from local curvature, which leads to motion binormal to the curve — in the case of a vortex ring, drift perpendicular to the plane it lies in, a feature shared by the rings studied here

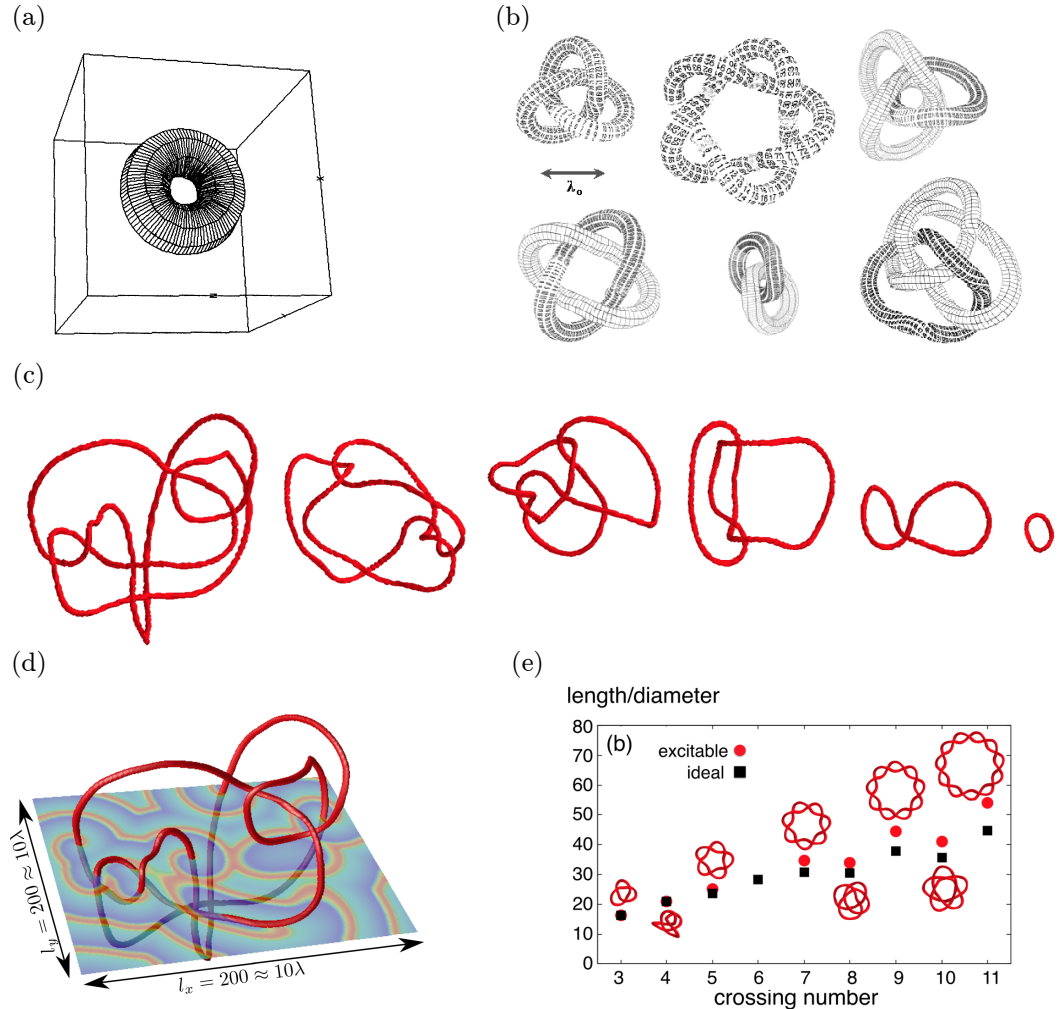


Figure 1.19: Stable knotted vortices in the FitzHugh-Nagumo model. (a) A vortex ring contracts to a stable radius and drifts at constant velocity; its radius is $0.23\lambda_0$, where λ_0 is the wavelength of the spiral wave in the medium (see scale bar in panel (b)). (b) An assortment of apparently stable knotted and linked vortices found in Ref. [Henze, 1993]. The tube around the knots is of diameter λ_0/π . The stability of the trefoil knot and Hopf link were subsequently confirmed in Ref. [Sutcliffe and Winfree, 2003] (the others are, in fact, unstable in the bulk). (c,d) The FitzHugh-Nagumo dynamics are capable of simplifying a tangled, but unknotted, curve to the canonical round form of panel (a); panel (c) shows an example simplification, with a cross section through the vortex knot in panel (d) showing the wavefield. (e) Recently, stable forms for torus knots and the figure-eight knot were found. Their geometries are shown here, alongside their lengths as compared to ideal ropelengths. Figures reproduced from Ref. [Winfree, 1990, 2002; Maucher and Sutcliffe, 2016, 2017].

[Winfree, 1990]. Further, exact knotted solutions to the LIA *do* exist [Hasimoto, 1972; Kida, 1981], and one might have hoped something similar applied here. Note however that the LIA breaks down in fluids too, and further that the nature of the fields surrounding the vortices is quite different between the two cases. One crucial difference, as we shall see, is that in excitable media waves propagate without attenuation for potentially arbitrary distances, making a theoretical decoupling of distant segments of the knot difficult.

In summary, the questions posed above are not satisfactorily answered. Our attempts to explore them, with a focus on systematically testing knots for stability and exploring the importance of nonlocal filament interactions, form §???. The potential for experimentally accessible, and spontaneously stable, knotted fields is a major motivator for this work.

1.5 This thesis

This thesis is primarily about knotted fields in soft matter systems, systems that may be loosely characterised as those in which geometry plays a fundamental role, and which may undergo substantial deformations in response to external forces, changes in temperature etc. All three of the systems described above might be considered examples of soft matter systems. One might ask “why choose soft matter?” and we hope that our descriptions of the experimental possibilities of such systems provide an immediate answer. Their combination of rich geometric structure and experimental accessibility make them natural testbeds for exploring knotted fields in all their guises. In our focus on soft matter we have of course been selective, completely neglecting discussion of theoretical and computational advances in optics [Bode et al., 2017; Dennis and Bode, 2017], electromagnetism [Rañada, 1989, 1990, 1992; Irvine, 2010; Kedia et al., 2013, 2016; Arrayás et al., 2017; Kedia et al., 2018a] and high energy physics [Faddeev and Niemi, 1997; Houghton et al., 1998; Battye and Sutcliffe, 1998, 1999; Sutcliffe, 2007]. Even within the realm of soft matter we have been selective; fluids stand out as the first and most highly developed examples of knotted fields, and as such it was natural to discuss them. Beyond that, as well as important examples of knotted fields in their own right, our presentation of material on liquid crystals and excitable media serve as background and motivation for the research topics addressed in this thesis.

As for the research topics themselves, they fall under the broad heading of ‘investigations into knotted fields in soft matter’, but each is a distinct story. Primarily they were chosen simply in response to current interesting questions in

knotted fields. As for §??, Maucher and Sutcliffe’s paper on unknot simplification [Maucher and Sutcliffe, 2016] was published in 2016, and one might take it as marking renewed interest in questions around the FitzHugh-Nagumo model — there is a gap of 13 years between it and the last publication on the matter [Sutcliffe and Winfree, 2003]. Coupled with improved computational abilities¹¹, new ideas about knot initialisation, and the recent experiments we discussed in §1.4, it seems a natural time for new investigation. §?? is again a development of recent questions about the geometry and topology of liquid crystal gradients; our focus will be on the topology of bend distortions. As we have seen, more theoretical attention has been paid to orthogonal gradients and twist Beller et al. [2014]; Machon and Alexander [2016a]; Machon [2017] than to bend (however there is recent work on splay and bend in two dimensions [Niv and Efrati, 2018]) and it is natural to try and complete the picture. The recent discovery of twist-bend and splay-bend nematic phases, of which the first review was published in 2018 [Jákli et al., 2018], provides further motivation as a natural experimental setting for theoretical constructs, a role the cholesteric plays for twist. The content of §2, on theoretical constructions for initialising knotted vortices, is a little different: it initially arose out of a practical need to do just that in §??. Many other methods exist and will be discussed in §2, but in one way or another they did not suit our needs, either because the geometries of knot they allowed were restricted, or they were computationally problematic. In attempting to solve this practical problem, we were led to re-evaluate Maxwell’s work on the solid angle function [Maxwell, 1873], extending it to knots and discovering connections between the various different methods he proposes for constructing the function, as well as connections to modern work on curve framings, writhe etc. As a result, this chapter has a ‘half theoretical, half practical’ feel. Its content was subsequently used in the simulations presented in §?? and in constructing the self-linkings of bend zeros described in §??.

We now provide a more technical summary of the content of each chapter, with reference to the foregoing discussion.

§2: Maxwell’s Theory of Solid Angle and the Construction of Knotted Fields

This chapter addresses a question which cuts across particular systems, and has not been much discussed above: Theoretically, how should one construct a knotted field? In order to simulate a knotted superfluid vortex (figure 1.6), a knotted vortex in

¹¹Compare the description in Ref. [Henze, 1993] of running code on a CRAY supercomputer to my own experience on my laptop and the Warwick cluster.

the FitzHugh-Nagumo model (figure 1.19), or any other knotted system one needs a method of initialising a topologically correct configuration before running dynamics. For the above examples, this amounts to constructing a phase field $\phi \in S^1$ containing a phase singularity with the topology (and possibly geometry) of the desired knot.

In this chapter we propose the solid angle function of a link K , defined by Maxwell in his *A Treatise on Electricity and Magnetism* [Maxwell, 1873], as a natural solution to this problem. We provide a systematic description of this function as a means of constructing a knotted field for any curve or link in \mathbb{R}^3 . This is a purely geometric construction in which all of the properties of the entire knotted field derive from the geometry of the curve, and from projective and spherical geometry. We emphasise a fundamental homotopy formula as unifying different formulae for computing the solid angle. The solid angle induces a natural framing of the curve, which we show is related to its writhe Wr and use to characterise the local structure in a neighbourhood of the knot. Finally, we discuss computational implementation of the formulae derived, and give illustrations for how the solid angle may be used to give explicit constructions of knotted vortices in excitable media and knotted director fields around disclination lines in nematic liquid crystals. Part of the work in this chapter consists of an implementation of the methods described in C++: it may be found at <https://github.com/garethalexander/SolidAngle>

TODO:INCLUDE IN THE APPENDIX

§???: Bend Geometry in Liquid Crystals

TODO: FILL THIS IN

§???:Stable and Unstable Vortices in Excitable Media

In §1.4 we discussed the discovery of several apparently stable knotted vortices in the FitzHugh-Nagumo model, as well as the dynamics' remarkable ability to simplify unknots without reconnections. We also saw that the mechanisms underlying these phenomena are still ill-understood, and posed the following questions: What determines the dynamics of these vortices? How are reconnections avoided? What is the mechanism of knot untangling? Are all knots stable, and if so can we predict their shapes? This chapter is an exploration of these questions. We perform a systematic survey of the dynamics of all knots with at most eight crossings, establishing that the generic behaviour is of unsteady, irregular dynamics, with prolonged periods of expansion of parts of the vortex. We show that the mechanism for the length expansion is a long-range wave-slapping interaction. We also show that there

are stable vortex geometries for certain knots; in addition to the unknot, trefoil, and figure-eight knots reported previously, we have found stable examples of the Whitehead link and 6_2 knot. We give a thorough characterisation of their geometry and steady-state motion. For the unknot, trefoil, and figure-eight knots we greatly expand previous evidence that FitzHugh-Nagumo dynamics untangles initially complex geometries while preserving topology, and discuss the mechanisms at play.

Chapter 2

Maxwell’s Theory of Solid Angle and the Construction of Knotted Fields

2.1 Introduction

Knotted fields are three-dimensional textures of continuous media that encode in their structure a knotted curve, filament or family of field lines. Originating in Lord Kelvin’s speculations of atomic structure as knotted vortices in the aether [Thomson, 1867], they have since been experimentally realised in nodal lines of optical beams [Dennis et al., 2010], disclinations in nematic liquid crystals [Tkalec et al., 2011; Tasinkevych et al., 2014; Čopar et al., 2015], spinor Bose-Einstein condensates and fluid vortices [Kleckner and Irvine, 2013]. Concurrently, theoretical studies continue to flourish in classical field theory [Sutcliffe, 2007], electromagnetism [Kedia et al., 2013; Arrayás et al., 2017], superfluids [Kleckner et al., 2016] and excitable media [Maucher and Sutcliffe, 2016, 2017, 2018].

Central to theoretical advances are explicit constructions for knotted fields exhibiting different knot types, or other pertinent physical properties, such as helicity in fluid flows. Constructions for knots in electromagnetic fields have centred around the Hopf map and rational map generalisations of it, shear-free null congruences and twistor methods [Rañada, 1992; Kedia et al., 2013; Arrayás et al., 2017; Kedia et al., 2018a]. The simplest constructions yield torus knots and links and the majority of constructions have focused on this family, together with seeking to control the helicity of the field [Kedia et al., 2018a], or its dynamics [Irvine, 2010]. The same rational map constructions also give knotted solutions in other field theo-

ries, such as the Skyrme-Faddeev model [Battye and Sutcliffe, 1998; Sutcliffe, 2007]. These methods satisfy the dynamical equations of motion directly and are geometrically special by construction, providing powerful tools for describing the full knotted field and its properties.

A separate approach has been developed to create nodal lines in optical beams that encodes the knot as the zero locus of a complex polynomial [Dennis et al., 2010]. From these fields initial conditions can be generated for paraxial wave equations with the subsequent evolution giving a beam containing the encoded knot. Again, the simplest constructions are for torus knots (captured by the polynomials $z_1^p + z_2^q$) but the method can be applied for any geometric braid [Bode et al., 2017; Dennis and Bode, 2017]. The argument of such a complex polynomial gives a phase field that winds around the knotted nodal line and can be used to initialise phase vortices, or as an angle orienting the director field of a liquid crystal with the nodal line then appearing as a disclination [Machon and Alexander, 2014]. In common with the constructions for electromagnetic knots, this approach encodes the knot implicitly rather than explicitly in that its location and geometry derives from the polynomial rather than being given *a priori*.

A canonical construction for a phase field associated to any knotted curve K , that depends only on the curve and represents a knotted field on its complement is given by the solid angle $\omega(\mathbf{x})$ subtended by K at each point in space. This construction of knotted fields goes back to Maxwell [Maxwell, 1873], since the solid angle is proportional to the magnetostatic potential of a current carrying wire, and in all likelihood represents the earliest explicit construction for a knotted field. If we imagine K to be a wire carrying unit current then Maxwell's equations state that it generates, in its complement, a magnetic field that is irrotational, so that locally it is the gradient of a potential. Ampère's law shows this potential to be globally multi-valued (increasing by μ_0 upon traversing any closed loop encircling the wire): the solid angle is the magnetostatic potential normalised to be 4π cyclic, i.e. it takes values in $\mathbb{R}/4\pi\mathbb{Z} \cong S^1$. This description makes clear that solid angle is naturally defined for an oriented curve K , the orientation being provided by the current flow. Since magnetic fields are divergence free, the solid angle is a harmonic function, and this, together with the 4π circulation, may be taken as an alternative definition. Knotted fields constructed out of it satisfy physical differential equations (Laplace's equation), but in contrast to other methods are more direct and explicit in their construction, so that there is no special focus on torus knots, geometric braids or any other particular class of knots.

Construction of the magnetostatic potential via numerical integration of the

magnetic field about K has recently been used to initialise knotted fields in superfluids and excitable media [Kleckner et al., 2016; Maucher and Sutcliffe, 2016]. However, very little in the way of a systematic treatment of solid angle and its geometric content has been given since Maxwell's own presentation in his *Treatise on Electricity and Magnetism* [Maxwell, 1873]. Maxwell devotes articles 417-422 of Ref. [Maxwell, 1873] to an extended discussion of solid angle, its properties and geometric meaning, as well as methods for calculating it. He gives three methods, in addition to (2.1): a direct calculation; a method given “for the sake of geometrical propriety”; and his preferred method which involves calculating the work done in transporting a unit magnetic pole to the point \mathbf{x} . Through the latter he (independently) derives the Gauss linking integral [Ricca and Nipoti, 2011].

Typically, solid angle is described with the help of an orientable surface Σ spanning K : $\omega(\mathbf{x})$ is then the area that this surface projects to on the unit sphere centred on \mathbf{x} , and is given explicitly by the formula [Saffman, 1992] (which Maxwell attributes to Gauss [Maxwell, 1873, Art. 409])

$$\omega(\mathbf{x}) = \int_{\Sigma} \frac{(\mathbf{x} - \mathbf{y})}{|\mathbf{x} - \mathbf{y}|^3} \cdot d\mathbf{S}, \quad (2.1)$$

where \mathbf{y} varies over Σ . While this description hides the fact that solid angle depends only on K , it provides the main geometric interpretation for solid angle and establishes close connections to projective and spherical geometry, particularly to spherical curves and areas. Solid angle, then, is a naturally geometric object dependent only on K , which involves an interplay between the geometry of K itself, and that of the spherical curve to which K projects. As such it belongs firmly to the domain of the differential geometry of curves. Yet its relationship to curve geometry is only partially developed, limited to how the local geometry influences the local structure of the magnetic field in the curve's normal plane [Saffman, 1992; Moore and Saffman, 1972; Ricca, 1994]. A related question is that of an ‘optimal’ method of computing ω , both from a theoretical and computational standpoint. Both methods mentioned above suffer deficiencies. In the first, an unnecessary intermediate, the magnetic field, is computed before ω . In the second, an arbitrary surface spanning K must be provided, of which ω is independent — this is especially inconvenient from a numerical standpoint. We desire a convenient direct expression for ω , dependent only on K .

In this paper, we show that Maxwell's three methods, extended where appropriate to knotted curves, may all be considered as applications of a single curve homotopy formula. In doing so, we shall arrive at several distinct formulae for com-

puting ω directly from K and make connections between solid angle and modern results on the geometry of spherical curves [Levi, 1994; Arnold, 1995], as well as discussing close connections between the asymptotic structure of ω and the writhe of K [Fuller, 1978; Dennis and Hannay, 2005]. With these formulae in place, we offer a geometric description of the local properties of ω in a tubular neighbourhood of K , considering both the structure in the normal plane and as one moves along the knot. Our description, which begins directly at the spherical geometry of the projected curve, complements existing results on the local structure of the magnetic field, and reveals a previously unseen connection between the local structure of ω and the ‘writhe framing’ of Ref. [Dennis and Hannay, 2005]. Our results give several formulae for the direct computation of ω from K , of practical value when initialising simulations of knotted fields. We discuss solutions to the main difficulties in their numerical implementation, and end with a brief description of applications to the initialisation of scroll waves in excitable media and knotted textures in nematics. Implementations in C of the methods described are given at github.com/garethalexander.

The extension of the construction of solid angle to the case where K is a link is straightforward: by the linearity of electromagnetism the solid angle for a link is simply the sum (mod 4π) of the solid angles corresponding to each of the link components. For this reason, we restrict the majority of our discussion to knots, and discuss the few subtleties which come with extension to links in a brief dedicated section.

2.2 The homotopy formula for solid angle

At each point \mathbf{x} of the knot complement the projection of K onto the unit sphere centred on \mathbf{x} , which we shall call the observation sphere, traces out a curve $\mathbf{n} := \frac{\mathbf{y}-\mathbf{x}}{|\mathbf{y}-\mathbf{x}|}$, $\mathbf{y} \in K$, as shown in figure 2.1. This projected curve has points of self-intersection in correspondence with the crossings of the knot as seen from \mathbf{x} . Upon varying \mathbf{x} there will be particular viewing points where the number of visible crossings changes and at those points \mathbf{n} also has cusps. In all cases (2.1) expresses that the solid angle at \mathbf{x} is the area bound by the projected curve \mathbf{n} on the observation sphere; indeed, Maxwell states this as the definition of the solid angle.

Maxwell’s first method of computing $\omega(\mathbf{x})$ is to choose arbitrary spherical coordinates (θ, ϕ) on the observation sphere, and integrate the projected area di-

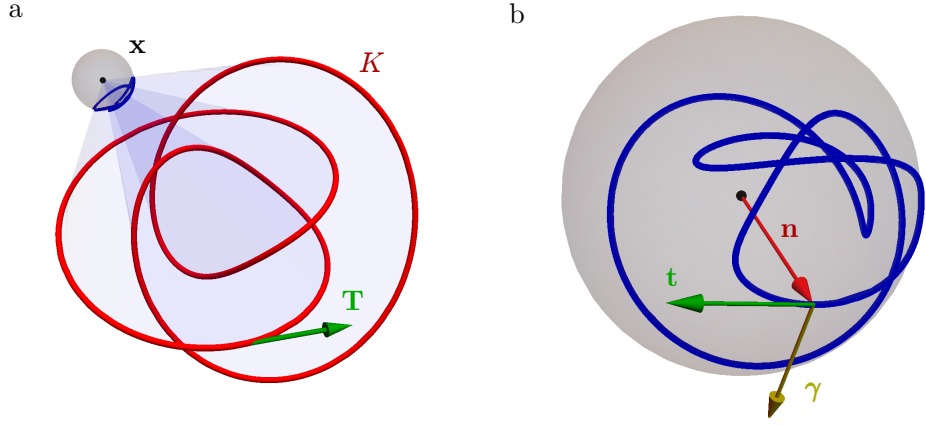


Figure 2.1: (a) An oriented knot K with tangent vector \mathbf{T} (here the 4_1) projects onto a unit observation sphere about a point \mathbf{x} , giving the spherical curve shown in blue. (b) The projection of K onto the observation sphere gives an immersed spherical curve \mathbf{n} , with self-intersections in correspondence with the crossings of the knot as seen from \mathbf{x} . A unit tangent \mathbf{t} for \mathbf{n} is induced by the orientation of K , and we select normal $\gamma := \mathbf{n} \times \mathbf{t}$.

rectly [Maxwell, 1873, Art. 417]:

$$\omega(\mathbf{x}) = \int (1 - \cos \theta) \, d\phi. \quad (2.2)$$

If we denote by \mathbf{n}_∞ the (arbitrarily chosen) polar direction $\theta = 0$, then (2.2) can be expressed in vector notation as

$$\omega(\mathbf{x}) = \int \frac{\mathbf{n}_\infty \times \mathbf{n}}{1 + \mathbf{n}_\infty \cdot \mathbf{n}} \cdot d\mathbf{n}, \quad (2.3)$$

a formula that has been rediscovered a number of times [Asvestas, 1985; Dangskul, 2015; M. Borodzik, 2017]. We remark that if we interpret (2.3) as an integral over K rather than its projection on the observation sphere, the integrand is the vector potential for a magnetic monopole placed at \mathbf{x} , with $-\mathbf{n}_\infty$ corresponding to the choice of Dirac string. Indeed, expressing it in the spherical coordinates of (2.2) we recover the vector potential of Ref. [Dirac, 1931]

$$\frac{\mathbf{n}_\infty \times \mathbf{n}}{1 + \mathbf{n}_\infty \cdot \mathbf{n}} \cdot \frac{1}{|\mathbf{y} - \mathbf{x}|} = \frac{\sin \theta}{r(1 + \cos \theta)} \hat{\phi}, \quad (2.4)$$

where $r = |\mathbf{y} - \mathbf{x}|$. Maxwell gives this formula explicitly in Cartesian coordinates and remarks on the role of the string (“axis”) in evaluating the integral.

Maxwell does not advocate the use of (2.2), other than for computational convenience, writing that it “involves a choice of axes which is to some extent arbitrary, and it does not depend solely on the closed curve” [Maxwell, 1873, Art. 418]. We shall discuss his second method in §2.3, but his preferred method is his third “as it employs no constructions which do not flow from the physical data of the problem” [Maxwell, 1873, Art. 419]: viewing ω as the magnetostatic potential of K , it may be built by measuring the change $\Delta\omega$ as we transport a unit magnetic pole along an arbitrary path from a reference location to \mathbf{x} , or equivalently by fixing \mathbf{x} and oppositely transporting K . Maxwell gives a formula for $\Delta\omega$ under this transport in terms of a double integral over the path and K , by summing the areas of the infinitesimal parallelograms swept out by line elements of K .

This approach shifts the focus from calculating the solid angle directly to calculating the change induced by a translation of the knot along some path. It is a small step to extend this to give a formula for the change associated to a general homotopy of K , in which the shape of K may vary. Of course, $\Delta\omega$ does not depend on the precise form of this homotopy, which allows it to be calculated using a standardised method, for instance by connecting corresponding points of the initial (K_0) and final (K_1) curves with straight lines, *i.e.* $K_t = (1-t)K_0 + tK_1$, $t \in [0, 1]$. This homotopy induces one on the observation sphere, which we denote \mathbf{n}_t , with the straight lines along which the points of K move projecting to geodesic arcs connecting \mathbf{n}_0 and \mathbf{n}_1 . The change in solid angle is the area swept out by this mesh of geodesic arcs.

Consider the contribution to the area of the geodesics connecting a small segment of the two curves: By Archimedes’ theorem on the equality of the area of the sphere and its circumscribed cylinder this is equal to the product of the distance $|\mathbf{n}_0 - \mathbf{n}_1|$ between the two endpoints of the geodesic arc and the angle swept out by its midpoint $(\mathbf{n}_0 + \mathbf{n}_1)/|\mathbf{n}_0 + \mathbf{n}_1|$. The difference in solid angle is therefore

$$\begin{aligned} \omega(\mathbf{x}; K_1) - \omega(\mathbf{x}; K_0) &= \int (\mathbf{n}_0 - \mathbf{n}_1) \times \frac{\mathbf{n}_0 + \mathbf{n}_1}{|\mathbf{n}_0 + \mathbf{n}_1|} \cdot d \frac{\mathbf{n}_0 + \mathbf{n}_1}{|\mathbf{n}_0 + \mathbf{n}_1|} \\ &= \int \frac{\mathbf{n}_0 \times \mathbf{n}_1 \cdot (d\mathbf{n}_0 + d\mathbf{n}_1)}{1 + \mathbf{n}_0 \cdot \mathbf{n}_1} \mod 4\pi. \end{aligned} \quad (2.5)$$

This is the basic homotopy formula for solid angle, applicable to an arbitrary deformation of K . Both Maxwell’s first and third methods of computing ω can be seen as applications of (2.5) — we recover (2.3) by letting K_0 recede asymptotically far from \mathbf{x} , so that \mathbf{n}_0 is a single point \mathbf{n}_∞ on the observation sphere and $\omega(\mathbf{x}; K_0) = 0 \mod 4\pi$. In §2.3 we shall use a homotopy of K along its tangent developable surface to demonstrate that his second method also follows directly from the homotopy

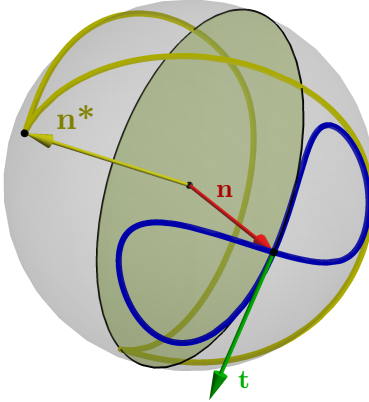


Figure 2.2: A spherical knot projection \mathbf{n} (blue curve, here a typical projection of a twisted unknot) induces a dual spherical curve $\mathbf{n}^* := \mathbf{t} \times \mathbf{n}$ (yellow curve). Maxwell proposes the construction of \mathbf{n}^* by allowing a unit circle (yellow disk) to roll without slipping around \mathbf{n} such that its plane of contact is tangent to \mathbf{n} . A unit vector perpendicular to this circle (yellow arrow) then traces \mathbf{n}^* . As shown in (2.9), zeros of geodesic curvature in \mathbf{n} correspond to cusps in \mathbf{n}^* (marked points). More pictures of this construction may be found in Refs. [Levi, 1994; Arnold, 1995].

formula.

The integral in (2.5) is not defined when \mathbf{x} lies on the surface swept out by K_t , which we refer to as the surface of discontinuity — as an example, in (2.3) this surface is formed by translating K to infinity along \mathbf{n}_∞ . The line of K_t passing through \mathbf{x} connects antipodal points of the observation sphere, $\mathbf{n}_0 \cdot \mathbf{n}_1 = -1$, and this line does not project to a unique geodesic arc connecting these endpoints. Instead there is a whole family of equivalent connecting geodesics, which cover the sphere once. As \mathbf{x} crosses the surface of discontinuity, the geodesic parameterisation of the antipodal sections of \mathbf{n}_0 and \mathbf{n}_1 jumps from one side of the observation sphere to the other, giving a 4π jump in (2.5).

We note that (2.5) has the same form as the formula given by Fuller for the difference in writhe of two curves [Fuller, 1978]. This is because for each fixed point \mathbf{x} (not on K_t for any t) the difference in solid angle is expressible as an area between two spherical curves, as arises for the difference in writhe. This is the first of several relations between the solid angle function for a curve and its writhe, which help to convey its geometric content.

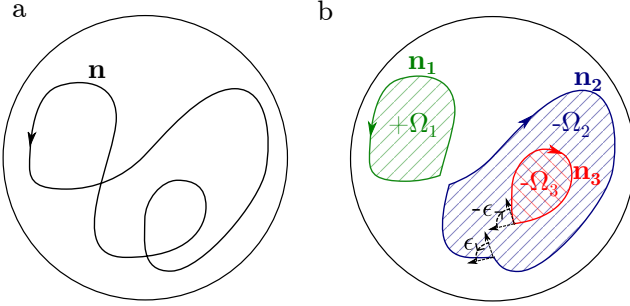


Figure 2.3: The spherical knot projection \mathbf{n} in panel (a) may be decomposed via the Seifert algorithm into Seifert circles \mathbf{n}_i , shown in panel (b). These circles bound regions Ω_i , signed according to the orientation of their boundary (coloured hatching). At self-intersection points of \mathbf{n} , the resulting circles have corners, with exterior angles ϵ_{ij} (shown for one such corner).

2.3 Maxwell's geometric formula, dual curves and homotopies along tangent developable surfaces

Maxwell's objection to (2.2) is that it involves an arbitrary choice of spherical coordinates on the observation sphere, and for this reason he states a construction in which no such choice is made [Maxwell, 1873, Art. 418]. Let a unit circle roll without slipping around \mathbf{n} such that its plane of contact is tangent to \mathbf{n} , as shown in figure 2.2. Then a unit vector perpendicular to this circle traces a second curve on the observation sphere, called the dual curve \mathbf{n}^* . Denote the length of \mathbf{n}^* by σ . Maxwell states that the solid angle is given by

$$\omega(\mathbf{x}) = 2\pi - \sigma, \quad (2.6)$$

a result he simply describes as a “well-known theorem”. This result is in fact equivalent to the Gauss-Bonnet formula [Lee, 1996], an identification that has been rediscovered at least twice [Levi, 1994; Arnold, 1995]. In the form stated by Maxwell, (2.6) is only correct if \mathbf{n} is a simple curve without points of inflection, but it is true in much greater generality [Arnold, 1995]. As a more general version is essential for application to generic knot projections, we give a self-contained elementary proof, applicable to any smoothly immersed spherical curve.

2.3.1 A dual curve theorem for self-intersecting curves

We begin by relating the area swept out by \mathbf{n} to its integrated geodesic curvature by using the Gauss-Bonnet formula. \mathbf{n} has a canonical tangent vector induced from the orientation of K , denoted \mathbf{t} , and we choose for it a normal vector $\gamma := \mathbf{n} \times \mathbf{t}$, as shown in figure 2.1(b). (Note that in the special case that \mathbf{n} is a simple curve it bounds two regions on the sphere, but is only correctly oriented as the boundary of one of them. γ points inwards to this region.) We perform a Seifert decomposition [Adams, 2004] of \mathbf{n} . This entails resolving each crossing in a manner that preserves the orientation of the curve and results in its separation into a collection of Seifert circles \mathbf{n}_i , as shown in figure 2.3. Each circle is a simple curve and bounds a region Ω_i . At self-intersections of \mathbf{n} the Seifert circles have corners, with exterior angles ϵ_{ij} . Now, for each circle, the Gauss-Bonnet formula tells us

$$\int_{\Omega_i} dA = 2\pi - \int_{\mathbf{n}_i} k_\gamma ds - \sum_j \epsilon_{ij}, \quad (2.7)$$

where $k_\gamma = \frac{d\mathbf{t}}{ds} \cdot \gamma$ is the signed geodesic curvature of the boundary. Summing over all Seifert circles, the left-hand-side gives $\omega(\mathbf{x}) \bmod 4\pi$; on the right-hand-side the exterior angles cancel pairwise, and we pick up a contribution of $2\pi S$, where S is the number of Seifert circles, in addition to the total integrated (signed) geodesic curvature. The number of Seifert circles is equal to $\chi + D$, where χ is the Euler characteristic of the surface constructed by the Seifert algorithm and D is the number of double points (self-intersections) [Adams, 2004; Lickorish, 1997]. For a knot the Euler characteristic of any Seifert surface is odd, so that $S = D + 1 \bmod 2$. Thus we have

$$\omega(\mathbf{x}) = 2\pi(D + 1) - \int_{\mathbf{n}} k_\gamma ds \bmod 4\pi. \quad (2.8)$$

We remark that the quantity $D + 1 \bmod 2$ is the spherical equivalent of the rotation number of a planar self-intersecting curve, sometimes termed its parity [Whitney, 1937; Phillips, 1966; Solomon, 1996]. The 2π in the Gauss-Bonnet formula arises as the rotation number of a simple curve, and the appearance of the parity here is thus a natural extension to the self-intersecting case.

The integrated geodesic curvature is equal to the (signed) length of the dual curve $\mathbf{n}^* := -\gamma = \mathbf{t} \times \mathbf{n}$ [Levi, 1994; Arnold, 1995](figure 2.2). To see this, consider how \mathbf{n}^* varies with arc length along \mathbf{n} :

$$\frac{d\mathbf{n}^*}{ds} = \frac{d}{ds}(\mathbf{t} \times \mathbf{n}) = \frac{d\mathbf{t}}{ds} \times \mathbf{n} = k_\gamma \mathbf{t}. \quad (2.9)$$

\mathbf{t} is tangent to \mathbf{n}^* , but its orientation alternates across zeros of k_γ , which correspond to cusps in \mathbf{n}^* . Defining $ds^* = k_\gamma ds$, we obtain $d\mathbf{n}^*/ds^* = \mathbf{t}$, and see that ds^* should be interpreted as a signed length element, the sign being given by that of k_γ . Thus we arrive at

$$\omega(\mathbf{x}) = 2\pi(D + 1) - \int_{\mathbf{n}^*} ds^* \mod 4\pi. \quad (2.10)$$

For a simple curve without inflection points $D = 0$ and the sign of ds^* never alternates, so its integral gives σ and we recover (2.6). By contrast, for \mathbf{n} as shown in figure 2.2 $D = 1$ and we have two zeros of geodesic curvature, which divide \mathbf{n}^* into two segments separated by cusps with ds^* switching sign between them. Applying (2.10) to this example gives the expected result $\omega = 0$; applying (2.6) does not. Eq. (2.10) thus generalises Maxwell’s “well known theorem” (2.6) to the case of a smoothly immersed curve, and in particular to any generic spherical knot projection.

2.3.2 The pullback to K and a homotopy along the tangent developable surface

As a result on the structure of spherical areas, (2.10) is valid for any spherical curve. However, we have in mind the case where one arises as the projection of the knot K . Using this projection we now pull each term in (2.10) back to K . This facilitates a reinterpretation in terms of the geometry of K , as well as a novel method of deriving it using (2.5).

We begin by constructing a natural ‘projective’ framing for K , dependent on \mathbf{x} , with which we will express D in (2.10) as a self-linking number. To construct this framing, extend the lines of sight from \mathbf{x} along \mathbf{n} until they meet K . These lines project to vectors normal to K , which are non-zero provided $\mathbf{n} \cdot \mathbf{T} \neq \pm 1$ where \mathbf{T} is the unit tangent vector to K , in other words provided there are no cusps in \mathbf{n} on the observation sphere. The number of double points seen from $\mathbf{x} \mod 2$ is equal to the self-linking number of K given this projective framing, $SL(K, \mathbf{x})$, also mod 2. The mod 2 counting gives an ambiguity in the sign of the identification of D with $SL(K, \mathbf{x})$ which will lead to two distinct re-writings of (2.10), and so we shall keep the sign explicit in the following.

Using Călugăreanu’s theorem [Călugăreanu, 1959, 1961], $SL(K, \mathbf{x}) = \text{Tw}(K, \mathbf{x}) + \text{Wr}(K)$, we now write $SL(K, \mathbf{x})$ in terms of the writhe of K and the twist of the projective framing, which is directly computed to be

$$\text{Tw}(K, \mathbf{x}) = \int_K \frac{(\mathbf{n} \cdot \mathbf{T})(\mathbf{n} \cdot \mathbf{T} \times d\mathbf{T})}{1 - (\mathbf{n} \cdot \mathbf{T})^2}. \quad (2.11)$$

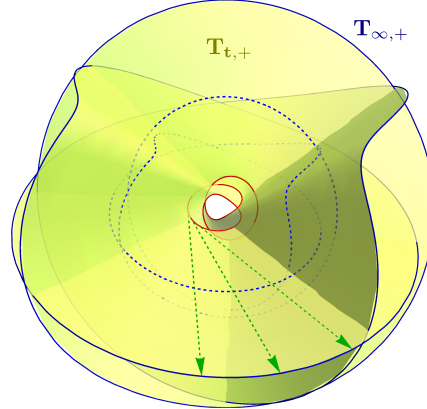


Figure 2.4: The forward tangent developable surface $\mathbf{T}_{t,+}$ (yellow surface) for the knot K in figure 2.1 (red curve), constructed by extending half-lines along tangents from K (green, dashed). The intersection of the surface with a sphere of asymptotically large radius gives a scaled copy of the tangent indicatrix to K , $\mathbf{T}_{\infty,+}$ (blue). The half-lines comprising $\mathbf{T}_{t,+}$ define a straight line homotopy between K and $\mathbf{T}_{\infty,+}$, from which the blue, dashed curve is taken.

Substituting this expression for $\text{SL}(K, \mathbf{x})$ into (2.10) with the sign ambiguity discussed above, and combining with the pullback of the dual curve length,

$$\int_{\mathbf{n}^*} ds^* = \int_{\mathbf{n}} k_{\gamma} ds = \int_K \frac{\mathbf{n} \cdot \mathbf{T} \times d\mathbf{T}}{1 - (\mathbf{n} \cdot \mathbf{T})^2}, \quad (2.12)$$

we arrive at

$$\omega(\mathbf{x}) = 2\pi(1 \pm \text{Wr}(K)) - \int_K \frac{\mathbf{n} \cdot \mathbf{T} \times d\mathbf{T}}{1 \pm \mathbf{n} \cdot \mathbf{T}} \mod 4\pi. \quad (2.13)$$

This formula for the solid angle depends only on K and data canonically associated to it, with the only ambiguity being a choice of sign. The appearance of the writhe in (2.13) reveals this geometric property of curves to be closely connected to the solid angle. We shall return to the sign ambiguity in a moment — for now, let us select the plus sign.

Instead of taking (2.6) as our starting point, we now demonstrate how (2.13) may be derived directly from the curve homotopy formula (2.5). To construct the appropriate homotopy, extend half-lines from K along its tangents \mathbf{T} , sweeping out a surface in space known as the forward tangent developable surface of K , which we denote $\mathbf{T}_{t,+} := \mathbf{y} + t\mathbf{T}$, $t \in [0, \infty)$ [Eisenhart, 1909] — an example of this surface is shown in figure 2.4. Consider the intersection of this surface with a sphere of asymptotically large radius. The curve $\mathbf{T}_{\infty,+}$ given by this intersection is simply

the spherical image of \mathbf{T} , known as the forward tangent indicatrix of K [Eisenhart, 1909], scaled to the sphere radius. Our desired homotopy is between $\mathbf{T}_{\infty,+}$ and K , and is defined by the half-lines comprising $\mathbf{T}_{t,+}$. As $\mathbf{T}_{\infty,+}$ is asymptotically far from \mathbf{x} , its projection on to the observation sphere simply reproduces the tangent indicatrix. Using the fact that $\mathbf{n} \times \mathbf{T} \cdot d\mathbf{n} = 0$, we see that the integral in (2.13) is a second special case of (2.5), with $K_0 = \mathbf{T}_{\infty,+}$, $K_1 = K$, and the area swept out on the observation sphere lying between the forward tangent indicatrix and \mathbf{n} .

This argument also identifies $2\pi(1 + \text{Wr}(K))$ as the solid angle of $\mathbf{T}_{\infty,+}$. We may obtain an integral formula for this area by considering the asymptotics of (2.13), allowing \mathbf{x} to recede far from K along $-\mathbf{n}_\infty$ so that $\omega(\mathbf{x}) \rightarrow 0$. Doing so yields

$$\int_K \frac{\mathbf{n}_\infty \cdot \mathbf{T} \times d\mathbf{T}}{1 + \mathbf{n}_\infty \cdot \mathbf{T}} = 2\pi(1 + \text{Wr}(K)) \mod 4\pi, \quad (2.14)$$

however, as this integral is the area bound by the tangent indicatrix on the unit sphere, the identification is simply a recovery of Fuller's writhe mod 2 formula [Fuller, 1978]. In the context of curve homotopies, we may interpret (2.14) as giving the change in solid angle for a homotopy in which $\mathbf{T}_{\infty,+}$ shrinks to a point (that projects to \mathbf{n}_∞ on the observation sphere). Eq. (2.13) may then be thought of as a combination of two homotopies: the first from an arbitrary point to $\mathbf{T}_{\infty,+}$, and the second from $\mathbf{T}_{\infty,+}$ to K . By contrast, (2.3) combines these two homotopies into one. Returning to the sign choice made above, we now see that choosing a minus sign would give a version of (2.13) corresponding to a homotopy along the backward tangent developable surface $\mathbf{T}_{t,-} := \mathbf{y} - t\mathbf{T}$, $t \in [0, \infty)$, between K and the backward tangent indicatrix $\mathbf{T}_{\infty,-}$. That aside, the geometric interpretation remains the same. We note briefly that the tangent indicatrix is not the only spherical curve canonically associated with K which might be used to define a homotopy; we might also consider the normal and binormal indicatrices. In these cases, however, neither triple product in (2.5) vanishes, as occurred in (2.13), and so the resulting formulae are less simple.

With the choice of plus (minus) sign in (2.13), the surface of discontinuity discussed in §2.2 is given by $\mathbf{T}_{t,+}(\mathbf{T}_{t,-})$. Jumps are also present in (2.8) and (2.10), however they occur on both halves of the tangent developable surface $\mathbf{T}_{t,+} \cup \mathbf{T}_{t,-}$ and the overall 4π jumps are composed of each individual term in the equations jumping by 2π . To convince ourselves of this fact, consider the behaviour of (2.10) as \mathbf{x} passes across $\mathbf{T}_{t,+} \cup \mathbf{T}_{t,-}$. \mathbf{n} undergoes a Reidemeister 1 move, during which D jumps by 1. The segment of \mathbf{n}^* corresponding to the Reidemeister move in \mathbf{n} begins and ends at antipodal points on the sphere. By removing the loop in \mathbf{n} , we

create two inflection points. Recalling that the sign of ds^* alternates between these inflections, we pick up a change in signed length of 2π .

2.4 The structure of ω

The level sets of ω , for regular values, form a family of Seifert surfaces with common boundary K . Figure 2.5 shows this global structure for a twisted unknot and a Whitehead link. The topology of the level sets changes at critical points of ω , where generically the local structure is a cone point $\pm(x^2 + y^2 - 2z^2)$ with Morse index 1 or 2. As the solid angle is a harmonic function, critical points of Morse index 0 or 3 are forbidden by the maximum principle. For knots and links that are fibred [Sta] it is possible for the solid angle to have no critical points at all; indeed this is the case for both the unknot and Whitehead link shown in figure 2.5. The general relationship between the shape and geometry of a knot or link and critical points of the solid angle is a fascinating open problem.

It is of particular interest to characterise ω in a tubular neighbourhood of K , so that we may modify it when initialising simulations using ω . This control is useful when the local structure of the field around a vortex affects its dynamics, as for example in helicity in fluids [Moffatt and Ricca, 1992] or the twist of scroll waves in the FitzHugh-Nagumo model [Winfree and Strogatz, 1984; Maucher and Sutcliffe, 2018]. This local structure has longitudinal and transverse parts: the level sets of ω rotate as one traverses K , and in a plane normal to K corrections due to local curvature and torsion arise, analogous to those studied for the magnetic field about a curved wire [Saffman, 1992]. Harmonic fields in the tubular neighbourhood of a knot have also recently been studied in Ref. [Duan and Yao, 2018].

2.4.1 Longitudinal structure — the solid angle framing

The intersection of the level set $\omega = 0$ with K defines a ‘solid angle’ framing, canonical in the sense that it depends only on the knot and is purely geometric. As this framing is described by a pushoff of K onto an orientable surface, it has zero self-linking number [Lickorish, 1997]; the extension to links is straightforward and discussed in § 2.5. Figure 2.6(a) shows this surface and its induced framing for the Whitehead link of figure 2.5. A natural question is to identify this solid angle framing in terms of the curve geometry. Let \mathbf{x} approach a particular point $\mathbf{y}(s) \in K$, for a fixed s , in such a way that the displacement vector $\mathbf{u} := \mathbf{x} - \mathbf{y}(s)$ defines a direction in the normal plane to the curve at s (figure 2.6(b)). Aligning the x, y, z axes with the local Frenet-Serret frame $\mathbf{N}(s), \mathbf{B}(s), \mathbf{T}(s)$, we have $\mathbf{u} = (\epsilon \cos \theta, \epsilon \sin \theta, 0)$. As

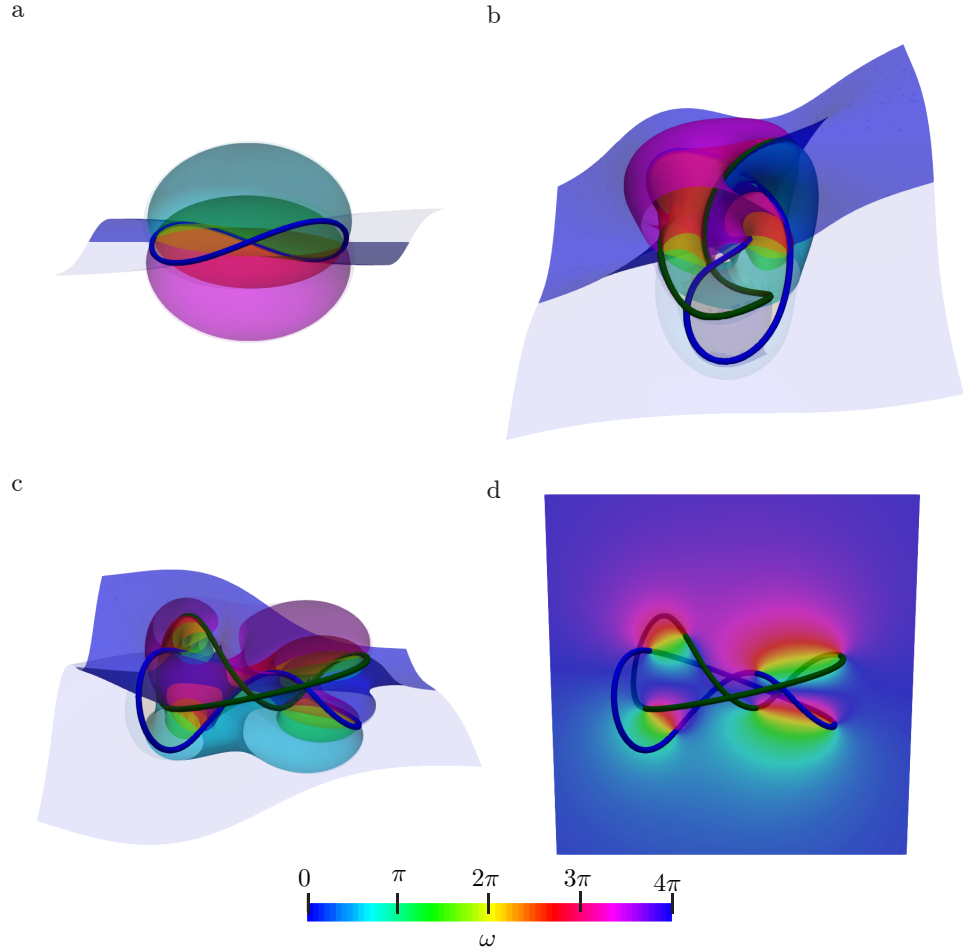


Figure 2.5: The structure of ω around a knotted curve, generated with the method of §2.5. (a)–(c) show level sets of ω of spacing $\frac{\pi}{2}$, each of which forms a Seifert Surface for the knot with opacities on the near sides of the images reduced to reveal the inner structure of ω . (a) A twisted unknot. (b,) (c) The Whitehead link (components in blue, green) from two viewing directions. (d) A slice through the Whitehead link from the same direction as (c). The local structure of ω about the knot is especially clear in (d) — ω winds by 4π , and as we move away from the knot, curvature induced corrections cause the level sets of ω to bunch along the curve normal, as discussed in §2.4.

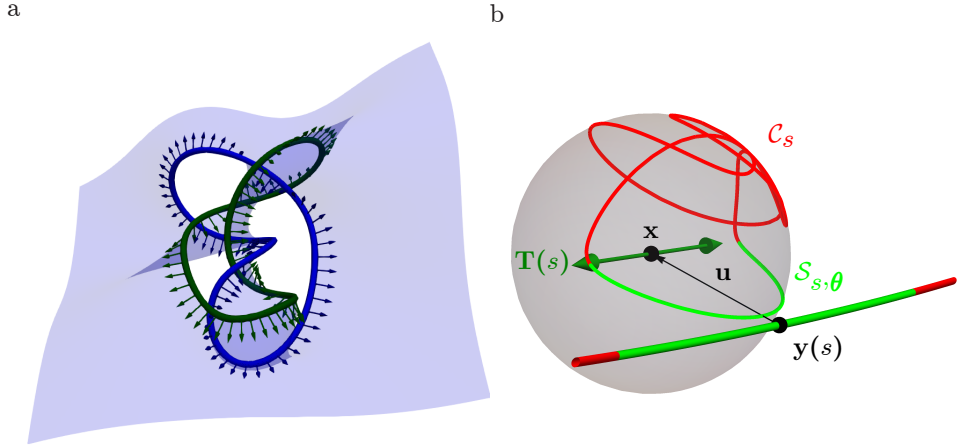


Figure 2.6: (a) The solid angle framing for the Whitehead link of figure 2.5. Shown is the level set $\omega = 0$ (blue surface), and its induced framing (components in blue, green). (b) The limiting behaviour of \mathbf{n} as \mathbf{x} approaches K (shown is the behaviour of \mathbf{n} about the marked point on the 4_1 of figure 2.1). \mathbf{x} approaches a fixed point $\mathbf{y}(s)$ on K such that $\mathbf{u} := \mathbf{x} - \mathbf{y}(s) = (\epsilon \cos \theta, \epsilon \sin \theta, 0)$ lies in the normal plane to $\mathbf{y}(s)$. As $\epsilon/\rho \rightarrow 0$, a region on K of size $\sqrt{2\rho\epsilon}$ (green) projects to a semicircle $\mathcal{S}_{s,\theta}$ between $\pm \mathbf{T}(s)$. This semicircle sweeps the observation sphere as θ is varied. The remainder of K projects to \mathcal{C}_s (red), and is independent of θ .

$\epsilon/\rho \rightarrow 0$, where ρ is the radius of curvature, we may think of the image of K on the observation sphere as comprised of two parts; for points $\mathbf{y}(s')$ with s' outside a small interval I around s (of size $\sim \sqrt{2\rho\epsilon}$), the projection to \mathbf{x} is no different from the projection to $\mathbf{y}(s)$, and the image of K is given by the unit chords $\frac{\mathbf{y}(s') - \mathbf{y}(s)}{|\mathbf{y}(s') - \mathbf{y}(s)|}$. This is a curve \mathcal{C}_s on the observation sphere with endpoints $\pm \mathbf{T}(s)$ and is independent of θ . In the same limit, the points $\mathbf{y}(s')$ with $s' \in I$ contribute to the image of K on the observation sphere a semicircle $\mathcal{S}_{s,\theta}$ between $\pm \mathbf{T}(s)$ with midpoint $-\frac{\mathbf{u}}{|\mathbf{u}|}$ that depends on θ . \mathbf{n} is thus decomposed as $\mathbf{n} = \mathcal{C}_s \cup \mathcal{S}_{s,\theta}$. Varying θ , \mathcal{C}_s remains unchanged, and $\mathcal{S}_{s,\theta}$ wraps the sphere once, giving the asymptotic winding structure $\omega = 2(\theta - \alpha(s))$, where $\alpha(s)$ is the rotation angle of the Frenet-Serret normal $\mathbf{N}(s)$ into the solid angle framing. $\alpha(s)$ gives the longitudinal structure of ω . It represents the contribution of \mathcal{C}_s to ω , and as such is a global quantity, not computable by a local analysis.

Our decomposition of \mathbf{n} is identical to that of the set of cross chords considered in the context of Călugăreanu's theorem [Dennis and Hannay, 2005; Călugăreanu, 1959], a consequence of the projection map outside of I degenerating to the chord

map as $\epsilon/\rho \rightarrow 0$ to give \mathcal{C}_s . The completion of \mathcal{C}_s by $\mathcal{S}_{s,\theta}$ is given, in Călugăreanu's theorem, by a choice of framing vector \mathbf{u} for K [Dennis and Hannay, 2005]. Here it is given, via projection, by the displacement vector \mathbf{u} .

As discussed by Dennis & Hannay in Ref. [Dennis and Hannay, 2005], given some framing \mathbf{u} , $\text{Wr}(K)$ and $\text{Tw}(K, \mathbf{u})$ are given by the areas swept out on an abstract sphere by \mathcal{C}_s and $\mathcal{S}_{s,\theta}$ respectively, as s varies along K . They point out that one may choose a special framing, which they call the ‘writhe framing’, such that the area swept out by $\mathcal{S}_{s,\theta}$ precisely cancels that swept out by \mathcal{C}_s , giving zero self-linking number. The discussion above makes clear this framing is exactly the solid angle framing, and the cancellation condition may be naturally read as a variation of θ such that $\frac{\mathbf{u}}{|\mathbf{u}|}$ lies tangent to the level set $\omega = 0$; in terms of the Frenet-Serret frame, $\theta = \alpha(s)$.

2.4.2 Transverse structure — curvature induced corrections to ω

In the previous section, we saw that the asymptotic structure of ω normal to K , corresponding to the decomposition $\mathbf{n} = \mathcal{C}_s \cup \mathcal{S}_{s,\theta}$, is simply $\omega = 2(\theta - \alpha(s))$. At finite ϵ/ρ we find corrections due to the local curvature of K , with the leading contribution being logarithmic in ϵ . For the derivative of ω , the magnetic field, this problem is well studied [Saffman, 1992; Ricca, 1994]. However, we wish to demonstrate that existing results may be mapped directly on to corrections in the geometry of \mathbf{n} as the decomposition $\mathbf{n} = \mathcal{C}_s \cup \mathcal{S}_{s,\theta}$ is smoothed at finite ϵ/ρ , insight one does not gain from the magnetostatic picture.

The asymptotic description $\mathbf{n} = \mathcal{C}_s \cup \mathcal{S}_{s,\theta}$ contains cusps at the boundary between \mathcal{C}_s and $\mathcal{S}_{s,\theta}$, located at $\pm\mathbf{T}(s)$. The primary effect of small but finite ϵ/ρ is a rounding of these cusps, and the displacement of \mathbf{n} slightly off $\pm\mathbf{T}(s)$, as shown in figure 2.7(a). It is thus natural to focus our attention, and chose coordinates, appropriate to describing \mathbf{n} in the vicinity of $\pm\mathbf{T}(s)$. Expanding $\mathbf{y}(s')$ to lowest order in s' , $\mathbf{y}(s') = (\frac{1}{2\rho}(s' - s)^2, 0, s' - s)$ and \mathbf{n} is given by

$$\mathbf{n} = \left[1 + \frac{\tilde{\epsilon}}{2} \left(\tilde{s}^2 + \frac{1}{\tilde{s}^2} \right) - \tilde{\epsilon} \cos \theta \right]^{-\frac{1}{2}} \left(\sqrt{\frac{\tilde{\epsilon}}{2}} \frac{1}{\tilde{s}} (\tilde{s}^2 - \cos \theta), -\sqrt{\frac{\tilde{\epsilon}}{2}} \frac{1}{\tilde{s}} \sin \theta, 1 \right), \quad (2.15)$$

where we have defined reduced lengthscales $\tilde{\epsilon} := \frac{\epsilon}{\rho}$, $\tilde{s} := \frac{s' - s}{\sqrt{2\epsilon\rho}}$. The form of (2.15) is chosen to emphasise that we have an expansion of \mathbf{n} in the vicinity of $\pm\mathbf{T}(s)$ on the observation sphere. Focusing now on the smoothed cusp at positive \tilde{s} , we introduce

a new variable $t := \ln(\tilde{s})$, and rotate the x - y coordinates of \mathbf{n} by $\frac{\theta}{2}$, yielding

$$\mathbf{n} = [1 + \tilde{\epsilon}(\cosh 2t - \cos \theta)]^{-\frac{1}{2}} \left(\sqrt{2\tilde{\epsilon}} \cos \frac{\theta}{2} \sinh t, -\sqrt{2\tilde{\epsilon}} \sin \frac{\theta}{2} \cosh t, 1 \right), \quad (2.16)$$

a hyperbola projected onto the observation sphere (figure 2.7(a)). In the original, unrotated coordinates, the asymptotic behaviour of this hyperbola is of two longitudinal great circles passing through $\mathbf{T}(s)$ at angles θ and 0. As $\tilde{\epsilon} \rightarrow 0$, the first of these circles gives $\mathcal{S}_{s,\theta}$. The second gives the local structure of \mathcal{C}_s , and in particular tells us that the direction of departure of \mathcal{C}_s from $\mathbf{T}(s)$ is set by $\mathbf{N}(s)$. The vertex of the hyperbola, found at $t = 0$, is the point of closest approach to $\mathbf{T}(s)$ and gives the natural choice $\tilde{s} = 1$ ($s' = s + \sqrt{2\rho\epsilon}$) to define the upper boundary between $\mathcal{S}_{s,\theta}$ and \mathcal{C}_s . It approaches the pole as $\sqrt{\tilde{\epsilon}}$, and so in the limit $\tilde{\epsilon} \rightarrow 0$ we recover the sharp decomposition $\mathbf{n} = \mathcal{C}_s \cup \mathcal{S}_{s,\theta}$.

The local structure of the solid angle can be computed using any of our formulae for ω , however, in view of the foregoing description, an appealing method is to use (2.8) and the geodesic curvature of the hyperbola. As this approach is symmetric in \tilde{s} , it is enough to compute the geodesic curvature for the hyperbola near $\tilde{s} = 1$ and simply double the result to account for $\tilde{s} = -1$. Further, the geodesic curvature of \mathbf{n} is strongly peaked in a localised region of size $\sim \sqrt{\tilde{\epsilon}}$ about the vertex of the hyperbola, decaying to 0 as the hyperbola approaches its asymptotic great circles. Using (2.16) we find an integrated geodesic curvature of

$$-2 \int_{-\infty}^{\infty} \frac{\sin \theta \sqrt{1 + \tilde{\epsilon}(\cosh 2t - \cos \theta)}}{\cos \theta + \cosh 2t + \tilde{\epsilon} \sin^2 \theta} dt, \quad (2.17)$$

where we have extended the upper limit of integration to $+\infty$, corresponding to an integration of the hyperbola between $-\frac{\mathbf{u}}{|\mathbf{u}|}$ and $\mathbf{N}(s)$ on the observation sphere. The integrand decays exponentially for large t so that the error involved is small.

The integral (2.17) may be evaluated exactly in terms of elliptic integrals of the first and third kind. The main feature is that the result is not analytic in $\tilde{\epsilon}$ but has leading behaviour $\tilde{\epsilon} \ln \tilde{\epsilon}$. This can be seen most easily by noting that the integrand decays exponentially for $|t| \gtrsim \frac{1}{2} \ln(2/\tilde{\epsilon})$ and that the integral is dominated by values of $|t|$ smaller than this. Retaining only the leading behaviour, one finds the local structure of the solid angle has the form

$$\omega(\tilde{\epsilon}, \theta) = 2(\theta - \alpha(s)) + \tilde{\epsilon} \ln \frac{8}{\tilde{\epsilon}} \sin \theta + O(\tilde{\epsilon}), \quad (2.18)$$

in which a zeroth order term from the integrated geodesic curvature gives the wind-

ing of ω and the logarithmic term causes the level sets of ω to bunch along the local normal. Figure 2.5(d) shows a cross-section through a Whitehead link in which both of these structures are clearly visible. In figure 2.7(b) we compare the various orders of approximation in (2.18) to the exact solution for a round unknot. In contrast to the divergence of the magnetic field, ω is perfectly well behaved as $\tilde{\epsilon} \rightarrow 0$. The logarithmic correction $\tilde{\epsilon} \log \tilde{\epsilon}$ tends to 0, but in a cusped manner, with unbounded radial derivative at the origin. We may interpret this fact as a direct consequence of the limiting cusped structure $\mathbf{n} = \mathcal{C}_s \cup \mathcal{S}_{s,\theta}$ — the magnetic field gives the rate of change in the area of a spherical curve as we smooth a cusp in it, and is thus naturally unbounded.

We note briefly that (2.18) is not harmonic — indeed, the corresponding expression for the magnetic field found in, for example, [Saffman, 1992] is not divergence free. This is a consequence of neglecting variation in ω along $\mathbf{T}(s)$ and one may verify that, allowing \mathbf{x} to lie off the plane normal to $\mathbf{y}(s)$, one picks up a term linear in z which restores harmonicity.

2.5 Remarks on numerical implementation, extension to links

In (2.3), (2.8), (2.10) and (2.13), we have several possible methods for computing ω for any curve K , directly from the specification of its embedding in \mathbb{R}^3 . The main difficulties in their numerical implementation are encountered when evaluating $\omega(\mathbf{x})$ at points close to the surface of discontinuity discussed in §2.2, 2.3.2. We shall focus discussion on (2.3) and (2.13), the remaining equations being of similar numerical character.

Focusing first upon (2.3), when \mathbf{x} lies on the surface of discontinuity it is pierced by a (generically) unique half-line extended from some point $\mathbf{y}(s) \in K$ such that $\mathbf{n}(s) \cdot \mathbf{n}_\infty = -1$. Considering the integral in (2.3) to be defined upon K , at the arc length s there is an isolated point of divergence in the integrand. In the degenerate case where \mathbf{x} lies upon a line of self-intersection in the surface, there will be multiple such points. Letting \mathbf{x} now lie slightly off the surface and approach it perpendicularly, we may expand the integrand of (2.3) using $\mathbf{x} - \mathbf{y}(s) := \epsilon \cos \theta \mathbf{n}_\infty + \epsilon \sin \theta \mathbf{n}_\infty \times \mathbf{T}(s)/|\mathbf{n}_\infty \times \mathbf{T}(s)|$, where θ is now the angle between $\mathbf{x} - \mathbf{y}(s)$ and the surface. We find that its limiting behaviour is that of a Lorentzian peak of width $\epsilon\theta$, which abruptly switches sign as \mathbf{x} crosses the surface. If one employs a simple numerical integration scheme with regularly spaced points along K of spacing Δs , the Lorentzian peak is not captured when $\epsilon\theta \approx \Delta s$. This leads to

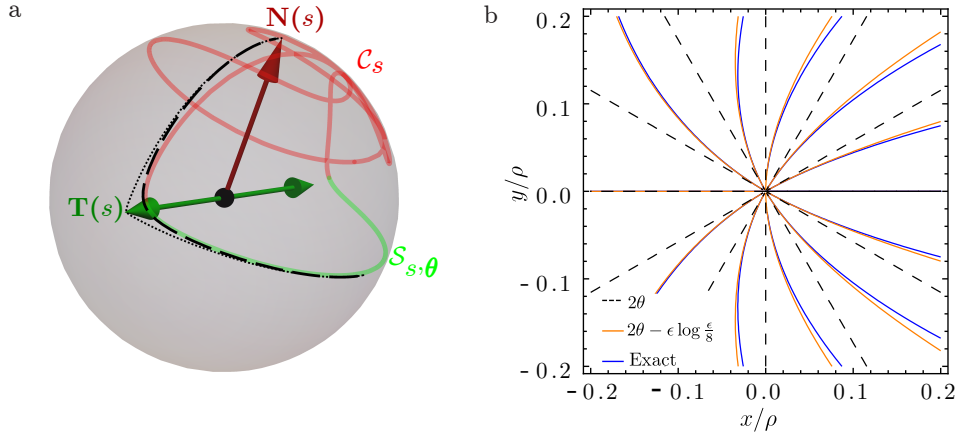


Figure 2.7: (a) For finite ϵ/ρ , the local structure of \mathbf{n} is approximated by the hyperbola (2.16) — the dashed black line gives the approximation to \mathbf{n} shown in figure 2.6. As $\epsilon/\rho \rightarrow 0$, the vertex of this hyperbola approaches $\mathbf{T}(s)$, and the asymptotes remain unchanged (black dotted line). In this way, we obtain the limiting decomposition $\mathbf{n} = \mathcal{C}_s \cup \mathcal{S}_{s,\theta}$. The two asymptotes are great circles through $\mathbf{T}(s)$ at angles θ and 0, and give the local behaviour of $\mathcal{S}_{s,\theta}$ and \mathcal{C}_s — note that that an angle of 0 corresponds to the direction $\mathbf{N}(s)$. (b) The local structure of ω in a plane normal to K . Contours of spacing $\frac{\pi}{3}$ are shown for the the zeroth order rotational structure (black dashed line), the curvature induced correction (2.18) (green) and the exact solution for a circle of radius ρ (blue). The absolute values of the level sets are arbitrary, as we have discarded global information about \mathcal{C}_s in our local structure calculations. The primary effect of curvature is to bunch the level sets of ω along the local normal. Note that for the curvature induced correction we have fixed the regular values in (2.18) to zero by comparison with the exact solution for a circle [Saffman, 1992].

poor approximation of $\omega(\mathbf{x})$ in a region of constant thickness Δs about the surface of discontinuity. By refining K , we may reduce the thickness of this region — unsurprisingly, this result suggests that Δs should be on the order of the resolution one desires for ω .

A similar discussion holds for (2.13), for which the divergences of the integrand occur at s such that $\mathbf{n}(s) \cdot \mathbf{T}(s) = \pm 1$, depending on which homotopy is used. The width of the Lorentzian peak instead scales as $\rho(s)\theta$, and so the thickness of the region of poor approximation is $\Delta s\epsilon/\rho(s)$; in particular, we note that this thickness scales with viewing distance in (2.13), but not in (2.3).

One method of avoiding these peaks is to use the freedom in (2.3), (2.13) to move the surface of discontinuity about in space, ensuring \mathbf{x} is never too close to it when computing $\omega(\mathbf{x})$. In (2.3), we have freedom in our choice of \mathbf{n}_∞ . The surface of discontinuity is given by dragging K to infinity along \mathbf{n}_∞ , and two different choices of \mathbf{n}_∞ will give two such surfaces. If K is knotted, these surfaces must intersect, giving a set of curves on which a third choice of \mathbf{n}_∞ is needed. In practice, an initial choice of \mathbf{n}_∞ is often suggested by the geometry of the input knot, or is simply chosen to be a coordinate axis. When computing $\omega(\mathbf{x})$, one may record the minimum value of $\mathbf{n} \cdot \mathbf{n}_\infty$ and, if it crosses some user defined threshold, switch to using $-\mathbf{n}_\infty$ for the calculation at that point. On the set of lines where this second choice again crosses the threshold, a random choice of \mathbf{n}_∞ may be used. (2.13) faces analogous problems on the tangent developable surface. Here, we have freedom in whether to place the discontinuity on $\mathbf{T}_{t,+}$ or $\mathbf{T}_{t,-}$. However, these two surfaces again generically intersect [Cle; Mond, 1989], and there is now no more freedom in (2.13), forcing one to either switch method or analytically correct for the Lorentzian peaks along such intersections. For this reason, and for the scaling properties discussed above, from a numerical standpoint we have found the use of (2.3) to be more convenient than (2.13).

Two brief computational remarks: As discussed in §2.4, the limiting local structure of ω about K has cylindrical symmetry. If one desires high accuracy to sample the tubular neighbourhood of K , one may use a cylindrical mesh out to a distance $\sim\rho(s)$. Finally, we note that as values of ω for different values of \mathbf{x} are computed independently of one another, our formulae are easily parallelised.

2.5.1 Extension to links

Extending our results to links is straightforward: by the linearity of electromagnetism, one simply sums $\omega \bmod 4\pi$ for each component of K . We reiterate that ω is only defined for oriented curves, and that different choices of orientation for each

component of K will give distinct solid angle functions. In the case of the solid angle framing discussed in §2.4, each component K_i acquires a framing, whose self-linking number equals the negative of the sum of the linking numbers between K_i and K_j , $j \neq i$ (figure 2.6).

2.6 Construction of knotted fields: two illustrations

We describe briefly two different examples of knotted fields that can be constructed using the solid angle as illustrations of how it influences the structure in different settings.

2.6.1 Scroll waves in excitable media

The possibility of knotting in the waves of excitable media has been considered for some time [Winfree and Strogatz, 1983a, 1984]. In a three-dimensional excitable medium, scroll waves of excitation emanate from a vortex filament, which it is possible to close into a loop or knot. Recent results have highlighted a remarkable topology-preserving dynamics in these materials [Maucher and Sutcliffe, 2016, 2017, 2018] in which the geometric shape of the vortex filament relaxes and simplifies but without strand crossings, thus preserving the topology. Simple effective curve dynamics seem insufficient to capture the full behaviour, which depends also on interactions mediated by the global structure of the scroll waves. This structure can be captured, in part at least, using the solid angle.

Scroll waves emanate from a knotted vortex filament creating an outward propagating family of approximately equi-spaced wavefronts. A simplified description of this wave system is given by a phase field that both winds by 2π around the filament curve and increases linearly with distance from it. This behaviour is captured by the function

$$\psi(\mathbf{x}) = kd_K(\mathbf{x}) + \frac{1}{2}\omega_K(\mathbf{x}) \mod 2\pi, \quad (2.19)$$

where $\omega_K(\mathbf{x})$ is the solid angle of K , $d_K(\mathbf{x}) = \min_{\mathbf{y} \in K} |\mathbf{y} - \mathbf{x}|$ is the distance from \mathbf{x} to the curve K and k is a wavenumber. In figure 2.8(a) we show an example of the scroll waves generated by a simple unknotted vortex ring. Note that the way the wave surface attaches to the filament – *i.e.* the local spin rate of the scroll wave along the length of the filament – is determined by the solid angle and, in particular, given by the solid angle framing. Of course, the phase function (2.19) can be modified to vary this; the modulation can be thought of as a K -dependent

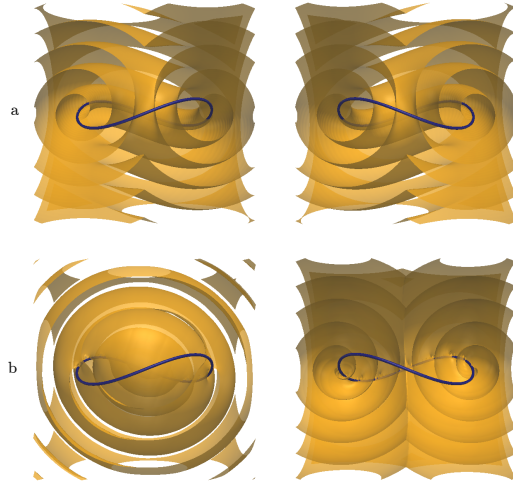


Figure 2.8: Scroll waves from an unknotted vortex filament. In (a) we show the zero level set of the phase field (2.19) and in (b) a modification of it where a sinusoidal modulation has been added to the solid angle framing, thereby adjusting the local spin rate of the scroll wave. In both (a) and (b) the two columns simply show different cuts through the emanating scroll waves.

off-set to the distance function $d_K(\mathbf{x})$. An example of such a modulation and how it alters the scroll waves is shown in figure 2.8(b).

2.6.2 Nematic disclinations

In nematic liquid crystals it is possible to manipulate topological defect lines, called disclinations, so as to create closed loops in the form of any knot or link [Tkalec et al., 2011; Čopar et al., 2015; Machon and Alexander, 2013]. The surrounding liquid crystal texture is an example of a knotted field. The molecular orientation in liquid crystals is described by a unit vector \mathbf{d} with the nematic symmetry $\mathbf{d} \sim -\mathbf{d}$; disclinations are line defects in the director field around which the orientation rotates by π , or reverses. The solid angle facilitates an explicit construction of a knotted field with this property. For example, the director field

$$\mathbf{d}(\mathbf{x}) = [\sin(\omega_K(\mathbf{x})/4), 0, \cos(\omega_K(\mathbf{x})/4)], \quad (2.20)$$

encodes K as a disclination line for any choice of knotted curve, or link. This knotted field has two particularly notable properties. First, since the solid angle is harmonic, it corresponds to a critical point of the one elastic constant Frank free energy. Second, the texture is “planar”, having no y -component.

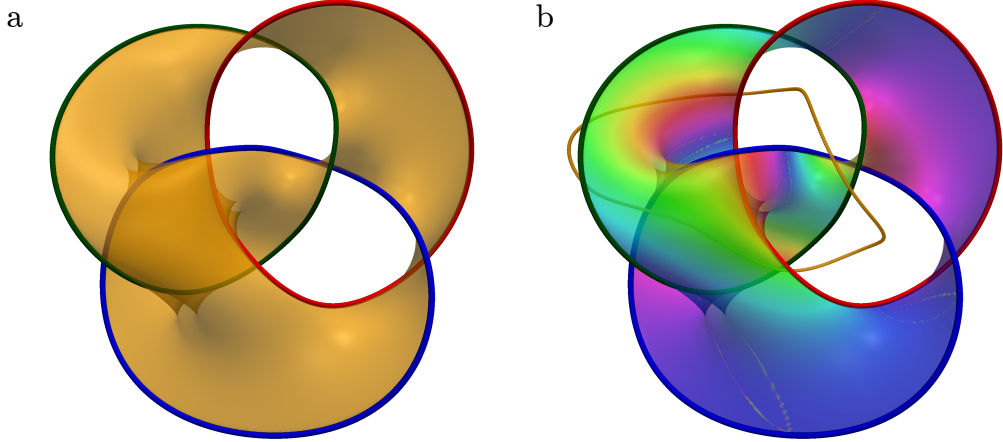


Figure 2.9: Knotted nematic texture for disclinations forming the Borromean rings. The surface corresponds to the set of points where the director has no z -component, $d_z = 0$; it is coloured according the xy -components. In (a) the texture is planar (Eq. (2.20)) and in (b) it is fully three-dimensional (the curve defining the xy -winding through the angle ω_L is also indicated).

We show in figure 2.9(a) a visualisation of the director field (2.20) for the case where the disclination lines K correspond to the Borromean rings. The knotted nematic texture is conveniently visualised by showing the surface where the z -component of the director vanishes — the vector field (2.20) has boundary conditions such that the director is aligned along z asymptotically far from K , motivating this choice. This surface is a level set of the solid angle, namely $\omega_K = 2\pi$.

A generalisation creating fully three-dimensional knotted nematics is the vector

$$\mathbf{d}(\mathbf{x}) = \left[\sin\left(\frac{\omega_K(\mathbf{x})}{4}\right) \cos\left(\frac{\omega_L(\mathbf{x})}{2}\right), \sin\left(\frac{\omega_K(\mathbf{x})}{4}\right) \sin\left(\frac{\omega_L(\mathbf{x})}{2}\right), \cos\left(\frac{\omega_K(\mathbf{x})}{4}\right) \right], \quad (2.21)$$

where $\omega_L(\mathbf{x})$ is a second solid angle function for a curve L chosen as follows. The surface $d_z = 0$ is the same as before (the level set $\omega_K = 2\pi$) but the director field is no longer constant over it, varying with the solid angle function ω_L . In figure 2.9(b) we illustrate this through the colour of the surface. Now the gradient of this colour is (proportional to) a magnetic field and L is the curve corresponding to the current carrying wire needed to generate that magnetic field. More formally, L is a curve in the complement of the surface $d_z = 0$ corresponding to a homology cycle and generates colour winding around the dual cycle of the surface itself. Knotted nematic

fields with any desired topological properties can be constructed in this way but of course the construction is more than purely topological and depends also on the geometric properties of the solid angle and of the curves that generate them.

2.7 Discussion

The solid angle provides a canonical knotted field for any explicitly given curve or link, depending only on that curve and its geometry. As such it facilitates a study of the geometry of knotted fields, shedding light on their structure and establishing connections between the field and the geometry of the curve. We have given a survey of its properties and methods for computing it that parallels and modernises Maxwell's seminal presentation. The fundamental result is the homotopy formula eq:Isotopy, which unifies the different formulae for calculating the solid angle, and also provides the means for characterising changes in the knotted field induced by deformations of the curve. In the latter context, it would be natural to study the consequences of inflection points and other geometric degeneracies in the curve shape, and also strand crossings or, with suitable extension, reconnections. Likewise, one could seek a characterisation of the geometric shape of a knot or link whose solid angle function realises specific properties, for instance having a minimal number of critical points. Those special geometric shapes where the properties of the solid angle change would then represent an interesting branch of singularity theory.

The local structure of the field can be considered particularly important in many systems. Here, the natural framing provided by the solid angle and its relation to the writhe of the curve establish a standard reference, from which the global effects of changes to the local behaviour can be systematically assessed.

Bibliography

- P. J. Ackerman and I. I. Smalyukh. Diversity of knot solitons in liquid crystals manifested by linking of preimages in torons and hopfions. *Phys. Rev. X*, 7: 011006, 2017.
- Colin C. Adams. *The knot book: An elementary introduction to the mathematical theory of knots*. American Mathematical Society, 2004.
- G. P. Alexander. Topology in liquid crystal phases. In S. Gupta and A. Saxena, editors, *The Role of Topology in Materials*. Springer International Publishing, 2018.
- G. P. Alexander, B. G. Chen, E. A. Matsumoto, and R. D. Kamien. Colloquium: Disclination loops, point defects, and all that in nematic liquid crystals. *Rev. Mod. Phys.*, 84:497–514, 2012.
- V. I. Arnold. The geometry of spherical curves and the algebra of the quaternions. *Russ. Math. Surv.*, 50:1–68, 1995.
- V. I. Arnold and B. A. Khesin. *Topological methods in hydrodynamics*. Springer, 1999.
- M. Arrayás, D. Bouwmeester, and J. L. Trueba. Knots in electromagnetism. *Phys. Rep.*, 667:1–61, 2017.
- J. S. Asvestas. Line integrals and physical optics. Part I. The transformation of the solid-angle surface integral to a line integral. *Journal of the Optical Society of America A*, (6):891, 1985.
- A. Azhand, J. F. Totz, and H. Engel. Three-dimensional autonomous pacemaker in the photosensitive belousov-zhabotinsky medium. *EPL*, 108:10004, 2014.

- T. Bánsági and O. Steinbock. Nucleation and collapse of scroll rings in excitable media. *Phys. Rev. Lett.*, 97:198301, 2006.
- R. A. Battye and P. M. Sutcliffe. Knots as stable soliton solutions in a three-dimensional classical field theory. *Physical Review Letters*, 81:4798–4801, 1998.
- R. A. Battye and P. M. Sutcliffe. Solitons, links and knots. *Proc. R. Soc. A*, 455: 4305–4331, 1999.
- D. A. Beller, T. Machon, S. Čopar, D. M. Sussman, G. P. Alexander, R. D. Kamien, and R. A. Mosna. Geometry of the cholesteric phase. *Phys. Rev. X*, 4:031050, 2014.
- V. N. Biktashev, A. V. Holden, and H. Zhang. Tension of organizing filaments of scroll waves. *Phil. Trans. R. Soc. A*, 347:611, 1994.
- B. Bode, M. R. Dennis, D. Foster, and R. P. King. Knotted fields and explicit fibrations for lemniscate knots. *Proc. R. Soc. A*, 473:20160829, 2017.
- R. Bott and L. Tu. *Differential forms in algebraic topology*. Springer-Verlag, 1982.
- B. G. Chen. *Topological defects in nematic and smectic liquid crystals*. PhD thesis, University of Pennsylvania, 2012.
- B. G. Chen, P. J. Ackerman, G. P. Alexander, R. D. Kamien, and I. I. Smalyukh. Generating the hopf fibration experimentally in nematic liquid crystals. *Phys. Rev. Lett.*, 110:237801, 2013.
- M. Courtemanche, W. Skaggs, and A. T. Winfree. Stable three-dimensional action potential circulation in the fitzhugh-nagumo model. *Physica D*, 41:173, 1990.
- G. Călugăreanu. L'intégrale de gauss et l'analyse des noeuds tridimensionnels. *Rev. Math. Pures Appl.*, 4:5–20, 1959.
- G. Călugăreanu. Sur les classes d'isotopie des noeuds tridimensionnels et leurs invariants. *Czechoslovak Math. J.*, 11:588–625, 1961.
- Supreedee Dangskul. *A Construction of Seifert Surfaces by Differential Geometry*. PhD thesis, University of Edinburgh, 2015.
- P. G. de Gennes and J. Prost. *The Physics of Liquid Crystals*. Oxford Science Publications, 1996.

- M. R. Dennis and J. H. Hannay. Geometry of călugăreanu's theorem. *Proc. R. Soc. A*, 461:3245–3254, 2005.
- M. R. Dennis, R. P. King, B. Jack, K. O'Holleran, and M. J. Padgett. Isolated optical vortex knots. *Nat. Phys.*, 6:118–121, 2010.
- Mark R. Dennis and Benjamin Bode. Constructing a polynomial whose nodal set is the three-twist knot 52. *J. Phys. A: Math. Theor.*, 50(26), 2017.
- H. Dierckx. *Dynamics of wave fronts and filaments in anisotropic cardiac tissue*. PhD thesis, The University of Ghent, 2010.
- P. A. M. Dirac. Quantised Singularities in the Electromagnetic Field. *Proc. R. Soc. A*, 133:60–72, 1931.
- M. DoCarmo. *Differential geometry of curves and surfaces*. Pearson, 1976.
- X. Duan and Z. Yao. Harmonic field in knotted space. *Phys. Rev. E*, 97, 2018.
- B. Echebarria, V. Hakim, and H. Henry. Nonequilibrium ribbon model of twisted scroll waves. *Phys. Rev. Lett.*, 96:098301, 2006.
- P. Comte ed. M. Tabor ed. ed. H. K. Moffatt ed., G. M. Zaslavsky ed. *Topological Aspects of the Dynamics of Fluids and Plasmas*. Springer, 1992.
- L. P. Eisenhart. *A Treatise on the Differential Geometry of Curves and Surfaces*. Ginn And Company, 1909.
- L. Faddeev and A. J. Niemi. Stable knot-like structures in classical field theory. *Nature*, 387:58–61, 1997.
- R. FitzHugh. Impluses and physiological states in theoretical models of nerve. *Bio-phys. J.*, 1:445–466, 1961.
- F. C. Frank. On the theory of liquid crystals. *Discuss. Faraday Soc.*, 25:19–28, 1958.
- F. B. Fuller. Decomposition of the linking number of a closed ribbon: A problem from molecular biology. Proc. Natl. Acad. Sci. USA, pages 3557–3561, 1978.
- D. S. Hall, M. W. Ray, K. Tiurev, E Ruokokoski A. H. Gheorghe, and M Möttönen. Tying quantum knots. *Nat. Phys.*, 12:478–483, 2016.
- R. Hänninen, N. Hietala, and H. Salman. Helicity within the vortex filament model. *Nat. Sci. Rep.*, 6:37571, 2016.

- H Hasimoto. A soliton on a vortex filament. *J. Fluid Mech.*, 51:477–485, 1972.
- A. Hatcher. *Algebraic Topology*. Cambridge University Press, 2002.
- H. Helmholtz. Über integrale der hydrodynamischen gleichungen, welche den wirbelbewegungen entsprechen. *J. fur die reine und angew Math*, 55:25–55, 1858.
- H. Henry and V. Hakim. Scroll waves in isotropic excitable media: Linear instabilities, bifurcations and restabilized states. *Phys. Rev. E*, 65:046235, 2002.
- C. Henze. *Vortex filaments in three dimensional excitable media*. PhD thesis, The University of Arizona, 1993.
- C. Henze and A. T. Winfree. A stable knotted singularity in an excitable medium. *Int. J. Bifurcat. Chaos*, 1:891, 1991.
- C. J. Houghton, N. S. Manton, and P. M. Sutcliffe. *Nucl. Phys. B*, 510(3):507–537, 1998.
- S. Čopar and S. Žumer. Nematic braids: Topological invariants and rewiring of disclinations. *Phys. Rev. Lett.*, 106:177801, 2011.
- W. T. M. Irvine. Linked and knotted beams of light, conservation of helicity and the flow of null electromagnetic fields. *J. Phy. A: Math. Theor.*, 43:385203, 2010.
- W.T.M. Irvine. Moreau’s hydrodynamic helicity and the life of vortex knots and links. *C. R. Mécanique*, 346:170–174, 2018.
- A. Jákli, O. G. Lavrentovich, and J. V. Selinger. Physics of liquid crystals of bent-shaped molecules. *Rev. Mod. Phys.*, 90:045004, 2018.
- N. Johnson. A visualization of the hopf fibration, 2011.
<https://nilesjohnson.net/hopf.html>.
- H. Kedia, I. Bialynicki-Birula, D. Peralta-Salas, and W. T.M. Irvine. Tying knots in light fields. *Phys. Rev. Lett.*, 111, 2013.
- H. Kedia, D. Foster, M. R. Dennis, and W. T. M. Irvine. Weaving knotted vector fields with tunable helicity. *Phys. Rev. Lett.*, 117:274501, 2016.
- H. Kedia, D. Peralta-Salas, and W. T. M Irvine. When do knots in light stay knotted? *J. Phy. A: Math. Theor.*, 51:025204, 2018a.

- Hridesh Kedia, Dustin Kleckner, Martin W Scheeler, and William T.M. Irvine. Helicity in superfluids: Existence and the classical limit. *Phys. Rev. Fluids*, 3: 104702, 2018b.
- J. P. Keener. The dynamics of three-dimensional scroll waves in excitable media. *Physica D*, 31:269, 1988.
- J. P. Keener and J. J. Tyson. The dynamics of scroll waves in excitable media. *SIAM Rev.*, 34:1, 1992.
- S Kida. A vortex filament moving without change of form. *J. Fluid Mech.*, 112: 397–409, 1981.
- D. Kleckner and W.T.M. Irvine. Creation and dynamics of knotted vortices. *Nat. Phys.*, 9:253–258, 2013.
- D. Kleckner, L. H. Kauffman, and W.T.M. Irvine. How superfluid vortex knots untie. *Nat. Phys.*, 12:650, 2016.
- S. Van Der Laan. The vortex theory of atoms. Master’s thesis, Utrecht University, 2012.
- J Lee. *Riemannian manifolds- An introduction to curvature*. Springer-Verlag, 1996.
- M. Levi. A “bicycle wheel” proof of the gauss-bonnet theorem, dual cones and some mechanism manifestations of the berry phase. *Expo. Math*, 12:145–164, 1994.
- W. B. R. Lickorish. *An Introduction to Knot Theory*. Springer-Verlag, 1997.
- S. J. Lomanaco. The modern legacies of thomson’s atomic vortex theory in classical electrodynamics. *AMS Proc. Symp. Appl. MathM*, 51:145–166, 1996.
- S. Dangskul A. Ranicki M. Borodzik. Solid angles and Seifert hypersurfaces. 2017. URL <http://arxiv.org/abs/1706.06405>.
- T. Machon. *Aspects of geometry and topology in liquid crystalline phases*. PhD thesis, University of Warwick, 2016.
- T. Machon. Contact topology and the structure and dynamics of cholesterics. *New J. Phys.*, 19:113030, 2017.
- T. Machon and G. P. Alexander. Knots and nonorientable surfaces in chiral nematics. *Proc. Natl. Acad. Sci. USA*, 110:4174–1417, 2013.

- T. Machon and G. P. Alexander. Knotted defects in nematic liquid crystals. *Phys. Rev. Lett.*, 113:027801, Jul 2014.
- T. Machon and G. P. Alexander. Global defect topology in nematic liquid crystals. *Proc. R. Soc. A*, 472, 2016a.
- T. Machon and G. P. Alexander. Umbilic lines in orientational order. *Phys. Rev. X*, 6:011033, 2016b.
- F. Maucher and P. Sutcliffe. Untangling knots via reaction-diffusion dynamics of vortex strings. *Phys. Rev. Lett.*, 116:178101, 2016.
- F. Maucher and P. Sutcliffe. Length of excitable knots. *Phys. Rev. E.*, 96:012218, 2017.
- F. Maucher and P. Sutcliffe. Rings on string in excitable media. *J. Phys. A: Math. Theor.*, 51:055102, 2018.
- J. C. Maxwell. *A Treatise on electricity and magnetism*. Cambridge University Press, 1873.
- N. D. Mermin. The topological theory of defects in ordered media. *Rev. Mod. Phys.*, 51:591–648, 1979.
- J. Milnor. *Topology from the differentiable viewpoint*. Princeton University Press, 1997.
- J. Milnor and J. D. Stasheff. *Characteristic classes*. Princeton university press, 1974.
- H. K. Moffatt. The degree of knottedness of tangled vortex lines. *J. Fluid Mech.*, 35:117–129, 1969.
- H. K. Moffatt. Helicity and singular structures in fluid dynamics. *Proc. Natl. Acad. Sci. U.S.A.*, 111:3663–3700, 2014.
- H. K. Moffatt and R. L. Ricca. Helicity and the călugăreanu invariant. *Proc. R. Soc. A*, 439:411–429, 1992.
- David Mond. Singularities of the tangent developable surface of a space curve. *Quart. J. Math.*, 40:79–91, 1989.
- D. W. Moore and P. G. Saffman. The motion of a vortex filament with axial flow. *Phil. Trans. R. Soc. Lond.*, 272:403–329, 1972.

- J. J. Moreau. Constantes d'un lot tourbillonnaire en fluide parfait barotrope. *R. R. Acad. Sci. Paris*, 252:2810–2812, 1961.
- J. Nagumo, S. Arimoto, and S. Yoshizawa. An active pulse transmission line simulating nerve axon. *Biophys. J.*, 50:2061–2070, 1962.
- I. Niv and E. Efrati. Geometric frustration and compatibility conditions for two-dimensional director fields. *Soft Matter*, 14:424–431, 2018.
- A Phillips. Turning a Surface Inside Out. *Sci. Am.*, pages 112–120, 1966.
- A. F. Rañada. A topological theory of the electromagnetic field. *Lett. Math. Phys.*, 18:97–106, 1989.
- A. F. Rañada. Knotted solutions of the maxwell equations in vacuum. *J. Phys. A: Math. Gen.*, 23, 1990.
- A. F. Rañada. On the magnetic helicity. *Eur. J. Phys.*, 13:70–76, 1992.
- R. Ricca. The effect of torsion on the motion of a helical vortex filament. *J. Fluid Mech.*, 273:241–259, 1994.
- R. L. Ricca and B. Nipoti. Gauss' linking number revisited. *J. Knot Theory Ramifications*, 20:1325–1343, 2011.
- P. G. Saffman. *Vortex Dynamics*. Cambridge University Press, 1992.
- Hayder Salman. Helicity conservation and twisted Seifert surfaces for superfluid vortices. *Proc. R. Soc. A*, 473:20160853, 2017.
- M .W. Scheeler, D. Kleckner, D. Proment, G. L. Kindlmann, and W. T. M. Irvine. Helicity conservation by flow across scales in reconnecting vortex links and knots. *Proc. Natl Acad. Sci. U.S.A.*, 111:15350, 2014.
- M. W. Scheeler, W. M van Rees, H. Kedia, D. Kleckner, and W. T. M. Irvine. Complete measurement of helicity and its dynamics in vortex tubes. *Science*, 357:487–491, 2016.
- J. V. Selinger. Interpretation of saddle-splay and the oseen-frank free energy in liquid crystals. *Liq. Cryst. Rev.*, 6:129–142, 2019.
- I. I. Smalyukh, Y. Lansac, N. A. Clark, and R. P. Trivedi. Three-dimensional structure and multistable optical switching of triple-twisted particle-like excitations in anisotropic fluids. *Nat. Mater.*, 9:139–145, 2010.

- B. Solomon. Tantrices of spherical curves. *Am. Math. Month.*, 103:30–39, 1996.
- P. M. Sutcliffe. Knots in the Skyrme-Faddeev model. *Proc. R. Soc. A*, 463:3001–3020, 2007.
- P. M. Sutcliffe and A. T. Winfree. Stability of knots in excitable media. *Phys. Rev. E.*, 68:016218, 2003.
- P. G. Tait. On knots i. *Trans. R. Soc. Edin.*, 28:145–190, 1876.
- P. G. Tait. On knots ii. *Trans. R. Soc. Edin.*, 32:327–342, 1883.
- P. G. Tait. On knots iii. *Trans. R. Soc. Edin.*, 32:493–506, 1884.
- M. Tasinkevych, M. G. Campbell, and I. I. Smalyukh. Splitting, linking, knotting, and solitonic escape of topological defects in nematic drops with handles. *Proc. Natl. Acad. Sci. U.S.A.*, 111:16268–16273, 2014.
- W. Thomson. On vortex atoms. *Proc. R. Soc. Edin.*, 6:94–105, 1867.
- U. Tkalec, M. Ravnik, S. Čopar, S. Žumer, and I. Muševič. Reconfigurable knots and links in chiral nematic colloids. *Science*, 333:62–65, 2011.
- J. F. Totz, H. Engel, and O. Steinbock. Spatial confinement causes lifetime enhancement and expansion of vortex rings with positive filament tension. *New J. Phys.*, 17:093043, 2015.
- J. L. Trueba and M. Arrayás. Vorticity field, helicity integral and persistence of entanglement in reaction-diffusion systems. *J. Phys. A: Math. Theor.*, 42:282001, 2009.
- L. Tu. *An introduction to manifolds*. Springer, 2010.
- S. Čopar, U. Tkalec, I. Muševič, and S. Žumer. Knot theory realizations in nematic colloids. *Proc. Natl. Acad. Sci. U.S.A.*, 112:1675–1680, 2015.
- H. Whitney. On regular closed curves in the plane. *Compositio Mathematica*, 4: 276–284, 1937.
- A. T. Winfree. Stable particle-like solutions to the nonlinear wave equations of three-dimensional excitable media. *SIAM Rev.*, 32:1–53, 1990.
- A. T. Winfree. *The geometry of biological time*. Springer, 2001.

- A. T. Winfree. A prime number of prime questions about vortex dynamics in non-linear media. In S. J. Hogan, A. R. Champneys, B. Krauskopf, M. di Bernardo and R.E. Wilson, H. M. Osinga, and M. E. Homer, editors, *Nonlinear Dynamics and Chaos: Where do we go from here?*, chapter 10. IoP, 2002.
- A. T. Winfree and S. H. Strogatz. Singular filaments organize chemical waves in three dimension: I. geometrically simple waves. *Physica D*, 8:35–49, 1983a.
- A. T. Winfree and S. H. Strogatz. Singular filaments organize chemical waves in three dimension: II. twisted waves. *Physica D*, 9:65–80, 1983b.
- A. T. Winfree and S. H. Strogatz. Singular filaments organize chemical waves in three dimension: III. knotted waves. *Physica D*, 9:333–345, 1983c.
- A. T. Winfree and S. H. Strogatz. Singular filaments organize chemical waves in three dimension: IV. wave taxonomy. *Physica D*, 13:221–233, 1984.
- L. Woltjer. A theorem on force-free magnetic fields. *Proc. Natl. Acad. Sci. U.S.A.*, 44:489–491, 1958.